TU Delft

Delft University of Technology

Document Version
Final published version

Licence
CC BY

Citation (APA)
Navarro, L. A., Fejer, B. G., Meriwether, J. W., Martinis, C., Zhang, S. R., Kerr, R., Souza, J. R., Siemes, C., Doornbos, E., & More Authors (2026). Thermosphere response to the May 2024 geomagnetic storm over the South American sector. *Frontiers in Astronomy and Space Sciences*, *Volume 13 - 2026*. https://doi.org/10.3389/fspas.2026.1830431

Important note
To cite this publication, please use the final published version (if applicable).
Please check the document version above.

Copyright
In case the licence states “Dutch Copyright Act (Article 25fa)”, this publication was made available Green Open Access via the TU Delft Institutional Repository pursuant to Dutch Copyright Act (Article 25fa, the Taverne amendment). This provision does not affect copyright ownership.
Unless copyright is transferred by contract or statute, it remains with the copyright holder.

Sharing and reuse
Other than for strictly personal use, it is not permitted to download, forward or distribute the text or part of it, without the consent of the author(s) and/or copyright holder(s), unless the work is under an open content license such as Creative Commons.

Takedown policy
Please contact us and provide details if you believe this document breaches copyrights.
We will remove access to the work immediately and investigate your claim.

This work is downloaded from Delft University of Technology.

frontiers
in Astronomy and
Space Sciences

TYPE Original Research
PUBLISHED 20 August 2026
DOI 10.3389/fspas.2026.1830431

Check for updates

OPEN ACCESS

EDITED BY
Ankush Bhaskar,
Vikram Sarabhai Space Centre, India

REVIEWED BY
Gilda De Lourdes González,
University of California Berkeley,
United States
Ana Caccavari,
National Autonomous University of
Mexico, Mexico

*CORRESPONDENCE
L. A. Navarro,
luis.navarro@colorado.edu

RECEIVED 14 March 2026
REVISED 15 July 2026
ACCEPTED 17 July 2026
PUBLISHED 20 August 2026

CITATION
Navarro LA, Fejer BG, Meriwether JW, Martinis C, Zhang SR, Kerr R, Souza JR, Scipion D, Siemes C, Doornbos E and Ponomarenko P (2026) Thermosphere response to the May 2024 geomagnetic storm over the South American sector. *Front. Astron. Space Sci.* 13:1830431. doi: 10.3389/fspas.2026.1830431

COPYRIGHT
© 2026 Navarro, Fejer, Meriwether, Martinis, Zhang, Kerr, Souza, Scipion, Siemes, Doornbos and Ponomarenko. This is an open-access article distributed under the terms of the Creative Commons Attribution License (CC BY). The use, distribution or reproduction in other forums is permitted, provided the original author(s) and the copyright owner(s) are credited and that the original publication in this journal is cited, in accordance with accepted academic practice. No use, distribution or reproduction is permitted which does not comply with these terms.

Thermosphere response to the May 2024 geomagnetic storm over the South American sector

L. A. Navarro[1]*, B. G. Fejer[2], J. W. Meriwether[3], C. Martinis[4], S. R. Zhang[5], R. Kerr[6], J. R. Souza[7], D. Scipion[8], C. Siemes[9], E. Doornbos[10] and P. Ponomarenko[11]

[1]Space Weather Technology, Research, and Education Center, University of Colorado at Boulder, Boulder, CO, United States, [2]Center for Atmospheric and Space Sciences, Utah State University, Logan, UT, United States, [3]Center for Solar-Terrestrial Research, New Jersey Institute of Technology, Newark, NY, United States, [4]Center for Space Physics, Astronomy Department, Boston University, Boston, MA, United States, [5]Haystack Observatory, Massachusetts Institute of Technology, Westford, MA, United States, [6]Computational Physics Inc., Lowell, MA, United States, [7]National Institute for Space Research, Sao Jose dos Campos, Brazil, [8]Jicamarca Radio Observatory, Geophysical Institute of Peru, Lima, Peru, [9]Delft University of Technology, Delft, Netherlands, [10]Royal Netherlands Meteorological Institute, De Bilt, Netherlands, [11]Institute of Space and Atmospheric Studies, University of Saskatchewan, Saskatoon, SK, Canada

We examined the thermospheric wind and temperature response over the South American sector during the main and early recovery phases of the 10–11 May 2024 geomagnetic superstorm. Our coordinated set of Fabry-Perot Interferometer (FPI), satellite-derived, and radar observations were obtained from observatories located at El Leoncito (Argentina, 31.8°S, 69.3°W), Cachoeira Paulista (Brazil, 22.7°S, 45°W), Santarém (Brazil, 2.4°S, 54.7°W), and Jicamarca (Peru, 11.96°S, 76.86°W), as well as from the Gravity Recovery and Climate Experiment Follow-On (GRACE-FO) 1 satellite. The observations reveal a prompt low-latitude response to the storm sudden commencement, characterized by strong upward and westward plasma drifts and nearly simultaneous westward neutral wind disturbances, followed by intense nighttime thermospheric perturbations with pronounced longitudinal and latitudinal variability. Zonal winds were initially weakly eastward over El Leoncito and strongly westward over Cachoeira Paulista before evolving to strongly westward and weakly eastward at early morning over each site respectively. Transhemispheric meridional wind surges of ~100 m/s at equatorial latitudes coincided with large-scale traveling ionospheric disturbances, while El Leoncito and Cachoeira Paulista exhibited mild meridional disturbances. Thermospheric temperatures were significantly enhanced throughout the night, with superimposed impulsive enhancements. These features are consistent with wind-field reorganizations and vertical motions, suggesting adiabatic processes associated with traveling atmospheric disturbances (TADs). These results provide new observational constraints on the low-latitude thermospheric response during an extreme geomagnetic storm and highlight the importance of neutral dynamics in storm-time thermosphere–ionosphere coupling.

KEYWORDS
adiabatic heating, disturbance winds, low latitude thermosphere ionosphere, neutral winds-plasma drifts, storm-time wind gradients, super geomagnetic storm, thermospheric temperature variations, travelling atmospheric disturbances

Highlights

- Disturbance winds and magnetospheric forcing jointly drove low latitude thermospheric disturbances
- Zonal thermospheric winds showed opposite evolution between west and east coast of South America
- Temperature variations across South America linked to wind convergence and vertical motion suggest adiabatic effects

1 Introduction

Geomagnetic storms are among the most significant drivers of variability in the coupled magnetosphere–ionosphere–thermosphere system. They occur when enhanced solar wind energy and momentum are transferred into Earth's magnetosphere through processes such as magnetospheric reconnection, particle precipitation, and intensified high-latitude currents. These storm-time geomagnetic conditions can drive strong global effects with time scales from minutes to days within the thermosphere-ionosphere system. This variability redistributes plasma globally, affecting satellite navigation and radio communications.

The resulting energy deposition, largely in the form of Joule heating at high latitudes, results in an overall increase of thermospheric temperature and generates a large-scale pressure gradient that drives a meridional global circulation commonly referred to as disturbance winds. The transport of angular momentum by these equatorward winds produces a westward subrotation of the wind field with respect to Earth. The resultant wind circulation drives ionospheric dynamo currents and storm-time polarization electric fields, ultimately producing a mid and low latitude current vortex opposite to the solar quiet current system. The combined action of the ionospheric disturbance dynamo drifts and thermospheric disturbance winds redistribute energy and momentum throughout the ionosphere-thermosphere system, resulting in significant changes in thermospheric circulation, composition, and vertical motion (e.g., Blanc and Richmond, 1980; Fuller-Rowell et al., 1994; Mazaudier and Venkateswaran, 1988; Richmond et al., 2003; Prolss, 1991; Paul et al., 2025; Tripathi et al., 2025). Similarly, impulsive storm-time Joule heating enhancements can also generate TADs, which propagate equatorward with phase speeds of several hundred meters per second while transporting heated neutral air far from their source regions. Ionospheric signatures of these processes are frequently observed as large-scale traveling ionospheric disturbances (LSTIDs), providing indirect tracers of the underlying neutral dynamics (Hunsucker, 1982; Shiokawa et al., 2002; Tsugawa et al., 2004).

Low- and equatorial-latitude coupling is particularly complex because of multiple mechanisms operating simultaneously on different time scales. Rapid changes in magnetospheric convection and substorm activity can produce prompt penetration electric fields that modify equatorial plasma drifts within minutes, leading to strong but short-lived electrodynamic responses (Fejer et al., 1979; Fejer and Scherliess, 1995; Fejer et al., 2008; Fejer and Navarro, 2022; Zhang et al., 2023). On the other hand, sustained high-latitude forcing drives disturbance winds and disturbance dynamo electric fields, which reorganize the global thermospheric circulation and strongly influence low-latitude ionospheric behavior from a few hours to days (Blanc and Richmond, 1980; Fejer et al., 2017; Navarro et al., 2019; Navarro and Fejer, 2020). The superposition of fast electrodynamic effects and slower neutral responses produces highly structured spatial and temporal variability, especially in the equatorial region.

Recent studies have emphasized storm-time thermospheric winds, temperature, and density responses over the equatorial region. Ground-based FPI observations have documented large departures from quiet-time wind and temperature patterns during geomagnetic storms (Meriwether et al., 2008; Navarro and Fejer, 2019; Zhang et al., 2015), while satellite measurements have shown that storm-time circulation and neutral density changes can persist long after geomagnetic indices begin to recover (Bruinsma and Forbes, 2010; Sutton et al., 2005; Xiong et al., 2015). Despite these advances, the relative roles of impulsive Joule heating, large-scale circulation reorganization, vertical transport, and their coupling to low-latitude ionospheric dynamics remain poorly quantified, particularly during extreme storm conditions.

The geomagnetic superstorm of 10–11 May 2024 was driven by successive Earth-directed coronal mass ejections and produced extreme solar wind and interplanetary magnetic field conditions, driving ionospheric and thermospheric disturbances on a global scale. Recent studies have reported magnetospheric and ionospheric responses during this storm, including intense auroral electrojet enhancements and supersubstorm activity, strong hemispheric asymmetries associated with large and rapidly varying interplanetary magnetic field (IMF), and an unprecedented poleward expansion and deformation of the equatorial ionization anomaly observed by space-based imagers (e.g., Hajra et al., 2025; Karan et al., 2024; Ohtani et al., 2025; Singh et al., 2024; Wang et al., 2025; Zhang et al., 2024). Wang et al. (2025) reported thermospheric wind disturbances of up to about 400 m/s over China measured by a network of midlatitude optical interferometers from the Chinese Meridian Project during the main phase of this storm. Recent studies have also highlighted outstanding electrodynamic features during this storm and emphasized that observed low-latitude disturbances cannot be fully explained by prompt penetration or classical disturbance dynamo mechanisms alone. For instance, Astafyeva et al. (2025) and Huang et al. (2025) argued that the ion-neutral coupling driven by neutral atmosphere processes are likely essential for explaining the observed ionospheric morphology and its prolonged recovery. However, direct observational studies of low latitude thermospheric responses during the 10–11 May 2024 superstorm remain scarce, particularly over the South American sector.

In this study, we examine the thermospheric response to the 10–11 May 2024 superstorm over the South American sector using coordinated ground-based and satellite observations. The following sections first describe the suite of instruments used in this study and the geomagnetic conditions. Next, we describe the horizontal wind field response measured by the FPIs and derived from GRACE-FO 1 satellite data, and the observed temperature response alongside detrended plasma density, and relative vertical winds observations from El Leoncito and Santarem. Later, we discuss multi-process storm-time effects on these parameters by integrating plasma drifts from the Jicamarca Incoherent Scatter Radar with empirical disturbance dynamo models. Ultimately, this work

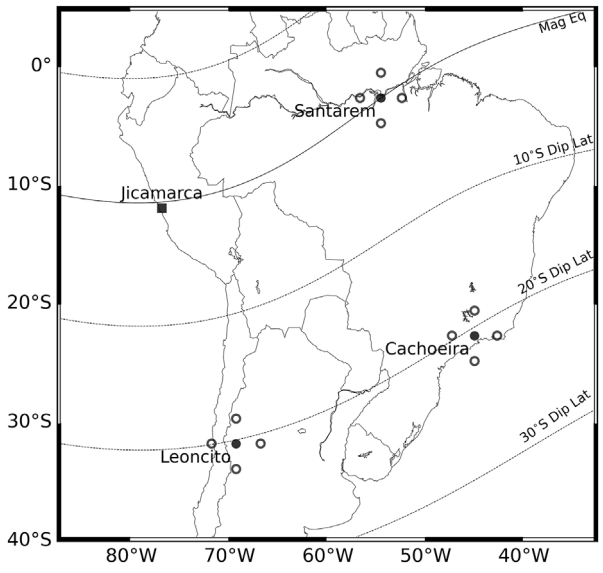

FIGURE 1
Geographic and geomagnetic locations of ground-based instruments used in this study. Filled black circles indicate FPI sites, open circles denote the thermospheric pierce points corresponding to line-of-sight observations at 45° elevation angle and 250 km emission altitude, The filled square indicates the Jicamarca Incoherent Scatter Radar.

seeks to advance the understanding of thermosphere–ionosphere coupling at low and equatorial latitudes providing new insights into three-dimensional neutral dynamics associated with one of the most intense geomagnetic storms on record.

2 Instruments and data

We characterized the upper atmosphere response to the 10–11 May 2024 geomagnetic superstorm using thermospheric wind and temperature observations from ground-based FPIs and cross-track thermospheric wind derived from the GRACE-FO 1 satellite data. These datasets were complemented with equatorial plasma drift measurements from the Jicamarca Incoherent Scatter Radar (ISR), Global Navigation Satellite Systems (GNSS) total electron content (TEC) maps and high-latitude convection maps derived from the Super Dual Auroral Radar Network (SuperDARN) observations. Together, these datasets enabled a coordinated investigation of storm-time thermosphere–ionosphere coupling during this extreme event. Figure 1 shows the geographic and geomagnetic locations of the FPIs and of the Jicamarca ISR.

We used FPI measured line-of-sight thermospheric neutral winds and temperatures from El Leoncito (Argentina, 31.8°S, 69.3°W; ~21°S magnetic latitude), Cachoeira Paulista (Brazil, 22.7°S, 45.0°W; ~22°S magnetic latitude), and Santarém (Brazil, 2.4°S, 54.7°W; magnetic equator), and also early-night thermospheric temperatures from the Jicamarca (Peru, 11.96°S, 76.86°W; magnetic equator) FPI. Together, these optical observatories provided coverage from low to equatorial latitudes across the South American sector. These instruments routinely monitor the thermalized bulk motion of atomic oxygen in the nighttime upper atmosphere. Throughout this study, abbreviated names will be also used to refer to the corresponding instrumentation and its observations.

The integration times were 120 s for the Leoncito FPI, 180 s for the Jicamarca FPI and 120 s for the Santarem and Cachoeira FPIs. The etalon clear aperture, spacer gap, and number of interferometric orders were 70 mm, 1.5 cm, and 10 for the Leoncito FPI; 75 mm, 1.5 cm, and 9 for the Jicamarca FPI; 100 mm, 1.0204 cm, and 4 for the Cachoeira FPI; and 100 mm, 1.0192 cm, and 4 for the Santarem FPI. The optical designs of the Jicamarca and Leoncito FPIs are described by Meriwether et al. (2011) and Martinis et al. (2025), respectively, while the Santarem and Cachoeira Paulista FPIs are described by Kerr et al. (2023).

Parameter estimation for data from the Jicamarca and Leoncito FPIs are described by Harding et al. (2014), whereas the procedures for the Santarem and Cachoeira FPIs are detailed in Kerr et al. (2023). In addition to horizontal winds, relative vertical winds were estimated using the nightly mean Doppler shift over each site as the rest position, under the assumption that the mean vertical motion is small and averages to zero across the night (Kerr et al., 2023; Meriwether et al., 2008). Therefore, only temporal variations in the inferred vertical winds are interpreted as geophysical signatures. Other factors that may influence vertical wind measurements and interpretation include atmospheric scattering and spectral contamination effects (e.g., Harding et al., 2017; Kerr et al., 2023). During the study period, raw spectra from vertical measurements at Santarem showed no evidence of spectral contamination, and the use of an ultra-narrow-band optical filter substantially reduces potential spectral contamination at El Leoncito. Also, inspection of raw spectra of vertical observations did not indicate evidence of atmospheric scattering of twilight glow before astronomical dusk and after astronomical dawn hours. Typical uncertainties during the study period were approximately 3 m/s for winds and 18 K for temperatures at El Leoncito, and 0.2 m/s and 17 K, respectively, at Cachoeira Paulista and Santarem.

Additional datasets used in this study are described below:

1. Cross-track thermospheric winds were estimated from accelerometer measurements of non-gravitational forces acting on the GRACE-FO 1 satellite by using aerodynamic drag and radiation pressure models. The retrieved cross-track winds represent large-scale neutral motions that are approximately horizontal and perpendicular to the satellite velocity vector. GRACE Follow-On missions consist of two spacecraft in a near-polar, near-circular low Earth orbit. During May 2024, the satellites operated at mean altitudes of approximately 475 km, with an orbital inclination of ~89° and an orbital period of ~95 min. In this study, thermospheric wind observations were obtained only from the GRACE-FO 1 satellite because the accelerometer onboard the second spacecraft exhibited elevated noise levels associated with an instrument anomaly. We used orbits segments covering the American sector, with solar local times primarily spanning the late afternoon and sunset hours. A detailed description of the GRACE-FO accelerometer data processing, aerodynamic force and radiation pressure modeling, wind and density retrieval

methodology, uncertainty estimates, and validation are provided by Hładczuk et al. (2024) and references therein.

2. Equatorial ionospheric plasma drifts were acquired by the Jicamarca Unattended Long-term Investigations of the Ionosphere and Atmosphere Medium Power (JULIA-MP; 11.95°S, 76.87°W; magnetic equator) radar during this period. The operational setup and technical comparisons with other operational modes are found in Fejer et al. (2024a), Flores et al. (2026) and Massoud et al. (2026). The experimental procedure and signal processing techniques to derive these drifts are described in Woodman (1970) and Kudeki et al. (1999) respectively. We removed nighttime observations exhibiting strong coherent power due to large-scale plasma irregularities. The remaining drifts were altitude-averaged using uncertainty weighting. The resultant vertical (zonal) drift uncertainties were ~1 m/s (~10 m/s) and ~8 m/s (~35 m/s) during daytime and nighttime, respectively, up to 04:00 UT on 11 May.
3. GNSS maps and differential TEC were derived by removing background variations using a Savitzky–Golay low-pass filter (Savitzky and Golay, 1964) with a 30-min sliding window and a linear basis function. The filter was applied to individual line-of-sight TEC measurements for each GNSS satellite–receiver pair. This methodology was introduced by Coster et al. (2017) and Zhang et al. (2017) and further detailed in Zhang et al. (2019). The detrended TEC data were subsequently used to construct a keogram in a magnetic latitude plane centered on the FPI site longitudes, using a longitudinal width of 6° and a latitudinal width of 1°. The resulting residuals were binned onto a grid of 0.5° in latitude and 2 min in UT hours, with cosine-latitude weighting applied to ensure near equal-area averaging toward the poles.
4. High-latitude ionospheric convection was characterized using Super Dual Auroral Radar Network (SuperDARN; Greenwald et al., 1995; Chisham et al., 2007; Nishitani et al., 2019). SuperDARN is a global network of high-frequency (10–18 MHz) coherent scatter radars that measure line-of-sight plasma drift velocities in the mid- and high-latitude ionosphere by observing backscatter from field-aligned ionospheric irregularities. These observations are fed into empirical plasma convection models yielding estimates of the large-scale two-dimensional ionospheric plasma convection and associated electrostatic potential distribution. These maps provide key parameters such as the cross polar cap potential, the spatial extent of the convection cells, and the equatorward boundary of high-latitude convection, commonly represented by the Heppner–Maynard boundary (HMB; Heppner and Maynard, 1987). During geomagnetic storms, SuperDARN convection maps capture the rapid expansion and intensification of ionospheric convection associated with enhanced solar wind–magnetosphere coupling, substorm current configurations, and variations in the interplanetary magnetic field. Detailed descriptions of the SuperDARN instrumentation, data processing, and convection mapping methodology are given by Chisham et al. (2007) and Ruohoniemi and Baker (1998), and references therein.

3 Results

3.1 Geomagnetic conditions

The first effects of the May 2024 geomagnetic storm started at 17:05 UT on 10 May 2024 when the shock arrival of the first of multiple and combined interplanetary coronal mass ejections significantly compressed the magnetosphere and subsequently disturbed the ionosphere and thermosphere system. Detailed descriptions of the solar wind, magnetospheric, and high latitude ionospheric conditions during this storm were given by Hajra et al. (2024), Hayakawa et al. (2024), Themens et al. (2024) and Tulasi Ram et al. (2024).

Figure 2 shows the evolution of solar wind and geomagnetic indices during the 10–11 May 2024 period. During this G5 geomagnetic storm, different geomagnetic indices exhibited sudden variations at 17:05 UT on 10 May, associated with the arrival of the first interplanetary coronal mass ejection (Hayakawa et al., 2024; Hajra et al., 2024). The SuperMAG Ring current (SMR) index increased by ~125 nT, while the Upper (SMU) and Lower (SML) Auroral Electrojet showed enhancements of ~800 nT and ~-1250 nT, respectively. At the same time, the Polar Cap South (North) index increased by ~20 (~14) mV/m, the SuperDARN North (South) Cross Polar Cap Potential (CPCP) increased by ~100 (~80) kV, indicating enhanced high-latitude plasma convection and magnetosphere-ionosphere coupling. Similarly, the Kp index reached 7+ from 15 to 18 UT on 10 May and later reached higher levels. The SMR later reached minimum values of −381 nT at ~22:28 UT on 10 May and −416 nT at ~02:14 UT on 11 May, reflecting the intense development of the storm-time ring current. It showed complex temporal variations associated with the arrival of multiple interplanetary shocks (Hajra et al., 2024).

Enhanced SMU and SML activity indicated repeated auroral electrojet intensifications and substorm activity during the storm main phase. Multiple substorm intensifications occurred between ~18:30 UT on 10 May and ~01:00 UT on 11 May, contributing to enhanced Joule heating and thermospheric forcing at high latitudes (Hajra et al., 2024; 2025). The Polar Cap North (PCN) and Polar Cap South (PCS) indices also showed strong geomagnetic activity following the shock arrival, with stronger magnitudes in the southern hemisphere between 17:05 UT and 18:30 UT on 10 May, comparable magnitudes in both hemispheres from 18:30 UT to 22:00 UT, and weaker southern hemisphere magnitudes between 23:00 UT on 10 May and 01:00 UT on 11 May. Similarly, the SuperDARN CPCP exhibited stronger magnitudes over the northern high-latitude convection pattern from 17:05 UT to 22:45 UT on 10 May, while both hemispheres showed generally comparable magnitudes during the remainder of the interval. The sustained enhancement of CPCP throughout the event is consistent with prolonged magnetospheric convection driven by strong solar wind–magnetosphere coupling. The Kp index further indicated persistent and intense geomagnetic activity, remaining above 8+ for most of the storm interval.

10.3389/fspas.2026.1830431

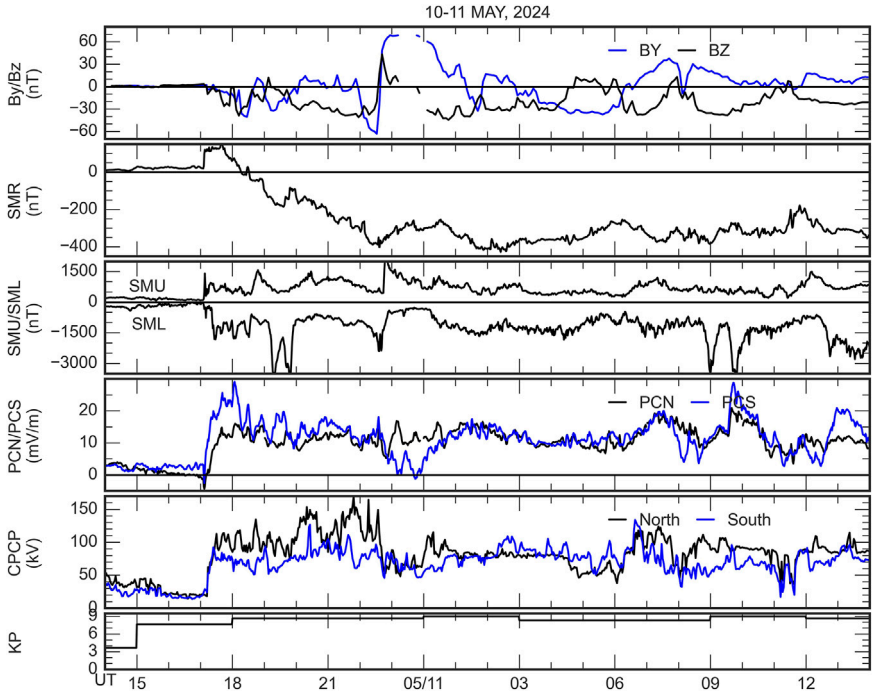

FIGURE 2
Solar wind parameters and Geomagnetic indices during the 10–11 May 2024 geomagnetic storm. (Top to bottom) Interplanetary Magnetic Fields By and Bz components, SuperMAG Ring Current (SMR), Auroral Electrojet Upper (SMU) and Lower (SML) indices, North and South Polar Cap indices, SuperDARN Cross Polar Cap Potential, and Kp index.

3.2 Thermospheric response over South America

Figure 3 shows the thermospheric neutral winds and temperatures over El Leoncito, Argentina (west coast) and Cachoeira Paulista and Santarem, Brazil (east coast) for the night of 10–11 May. The different colors correspond to different cardinal look directions with respect to the instrument site and for a 45° elevation except for the zenith look direction. For example, top panel shows the eastward winds observed along the East and West looking directions. The green solid line on each of these figures represents the quiet-time empirical representation derived using an average of quiet-time observations with average Kp < 2 for the previous 6 h. This approach to showing quiet time wind behavior is explained further by Navarro and Fejer (2020).

This figure shows that neutral winds and temperatures over Leoncito, Cachoeira and Santarem were strongly disturbed. The zonal wind response exhibited markedly different behavior over the West and East Coasts of South America. Early in the night, the zonal wind disturbance was strongest over the East coast with westward wind magnitudes of 150 m/s to the east of Cachoeira and 100 m/s to the west. These westward wind magnitudes slowly decreased and exhibited short-lived variations at 00:45 UT, 03:00 UT and 06:30 UT. The wind speed decreased from 100 m/s westward at 05:00 UT 11 May to near zero at 06:30 UT. After a brief period of westward flow, the wind reversed to eastward at ~08:30 UT. Thus, the East Coast experienced a progressive weakening of the initial westward disturbance followed by a reversal to eastward flow. Similarly, the West coast neutral winds over Leoncito started weakly eastward with wind speeds of ~40 m/s from 23:30 UT 10 May to 01:00 UT 11 May but then reversed, progressively increased toward the west and reaching 190 m/s (210 m/s) at 05:45 UT and 220 m/s (200 m/s) at 10:00 UT 11 May to the east (west) of Leoncito. In contrast to Cachoeira, Leoncito exhibited a continuous strengthening of the westward winds throughout the night, producing an opposite storm-time evolution between the West and East Coasts.

The wind field over Santarem started eastward during the early-night period and reversed westward at ~02:30 UT 11 May, increasing westward throughout the night. It exhibited short-lived eastward variations at 01:20 UT, 04:15 UT and 07:30 UT 11 May. At equatorial latitudes over the East coast, the zonal winds were 100 m/s eastward at 23:00 UT 10 May and exhibited decreasing velocities throughout the night with short-lived eastward variations at 01:30 UT, 04:00 UT and 07:30 UT. The eastward wind weakened to near-zero magnitudes at 00:00 UT 11 May, increased to 80 m/s eastward at 01:30 UT, and reversed to westward flow at 02:30 UT. These magnitudes continued increasing westward up to 80 m/s at 09:00 UT. The zonal wind evolution at Santarem was therefore similar to that observed at other equatorial sites, with strongest westward magnitudes in the midnight and post-midnight sectors, consistent with previous observations of storm-time equatorial wind disturbances (Navarro and Fejer, 2020). Superimposed on this large-scale trend, both locations exhibited three short-lived perturbations with amplitudes of approximately 50 m/s around 01:30 UT, 04:00 UT, and 07:30 UT.

10.3389/fspas.2026.1830431

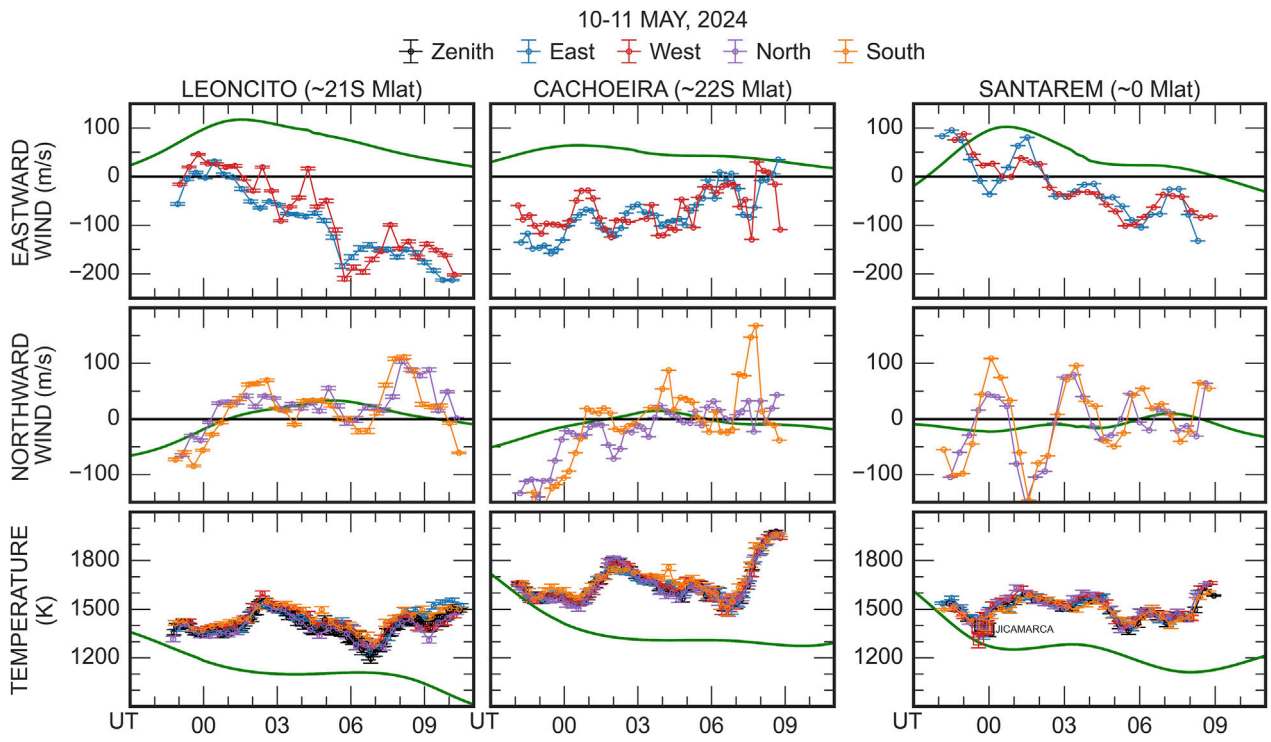

FIGURE 3
Thermospheric neutral winds and temperatures from the night of 10–11 May over El Leoncito, Argentina and Cachoeira Paulista and Santarem, Brazil. Early-night temperature observations over Jicamarca, Peru are shown along with Santarem observations. Line colors represent different cardinal looking directions for a 45° elevation except for the Zenith looking direction. Green solid lines represent quiet-time empirical references using Kp(0–6 hrs)<2 similar to Navarro and Fejer (2020). Typical wind and temperature uncertainties during this period were of 3 m/s and 18 K respectively for Leoncito FPI, and of 0.2 m/s and 17 K respectively for Cachoeira and Santarem FPIs. Local midnight occurs at 04:37 UT, 03:38 UT, 03:00 UT over El Leoncito, Cachoeira Paulista, and Santarem, respectively.

On the other hand, both sites of Leoncito and Cachoeira exhibited southward winds at early night that decreased to weakly northward from 01:00 UT up to early morning with northward surges at ~01:30 UT, ~05:00 UT, and ~08:00 UT (01:00 UT, 04:15 UT, 07:45 UT) over Leoncito (Cachoeira). These meridional wind perturbations occurred at approximately the same times as the zonal wind fluctuations, suggesting a common disturbance source. The wind field showed a southward gradient in both sites during the early-night and early-morning periods in both southern sites of Leoncito and Cachoeira. On the other hand, equatorial winds over Santarem showed strong interhemispheric disturbance wind surges throughout the night. These reached southward winds of 100 m/s, 150 m/s, 50 m/s and 50 m/s at 22:30 UT 10 May and 01:30 UT, 04:45 UT, 08:00 UT 11 May, and northward winds of ~100 m/s, 80 m/s, 50 m/s at 00:00 UT, 03:00 UT, 06:00 UT, 08:45 UT 11 May. They showed a slight southward gradient at ~02:00 UT followed by a strong southward gradient at 00:00 UT and 06:30 UT.

The thermospheric temperatures exhibited strongly enhanced magnitudes throughout the night of 10–11 May and followed similar temporal variations at all three sites, indicating a coherent regional response to the storm. Temperatures over Santarem remained near 1,500 K throughout the night and exhibited repeated enhancements with peak magnitudes at 01:00 UT, 03:30 UT, 06:30 UT and 08:30 UT 11 May. Similar early-night temperature variations were observed from the western equatorial site of Jicamarca, suggesting that the disturbance extended across a broad longitudinal sector. The low-latitude observations from Leoncito and Cachoeira also exhibited similar enhancements with temporal patterns similar to those observed at Santarem, although with larger magnitudes over Cachoeira. Superimposed on the elevated storm-time temperatures, both low-latitude sites exhibited several impulsive heating events, occurring near 02:30 UT, 04:30 UT, 05:15 UT, 10:00 UT over Leoncito and near 02:00 UT, 05:00 UT, and 08:00 UT over Cachoeira. These heating enhancements occurred approximately 60 and 40 min, respectively, after similar features observed at Santarém, suggesting a delayed response at low latitudes relative to the equatorial region.

3.3 Thermospheric wind response over low-latitude region

The thermospheric wind response from the east and west coasts of South America is further examined using cross-track eastward wind observations from the GRACE-FO 1 satellite. These observations are compared with solar wind and geophysical indices, as well as parameters derived from the SuperDARN high-latitude convection pattern estimations.

Figure 4 compares the interplanetary By and Bz magnetic fields, Polar Cap North and South indices, the Cross Polar Cap Potential

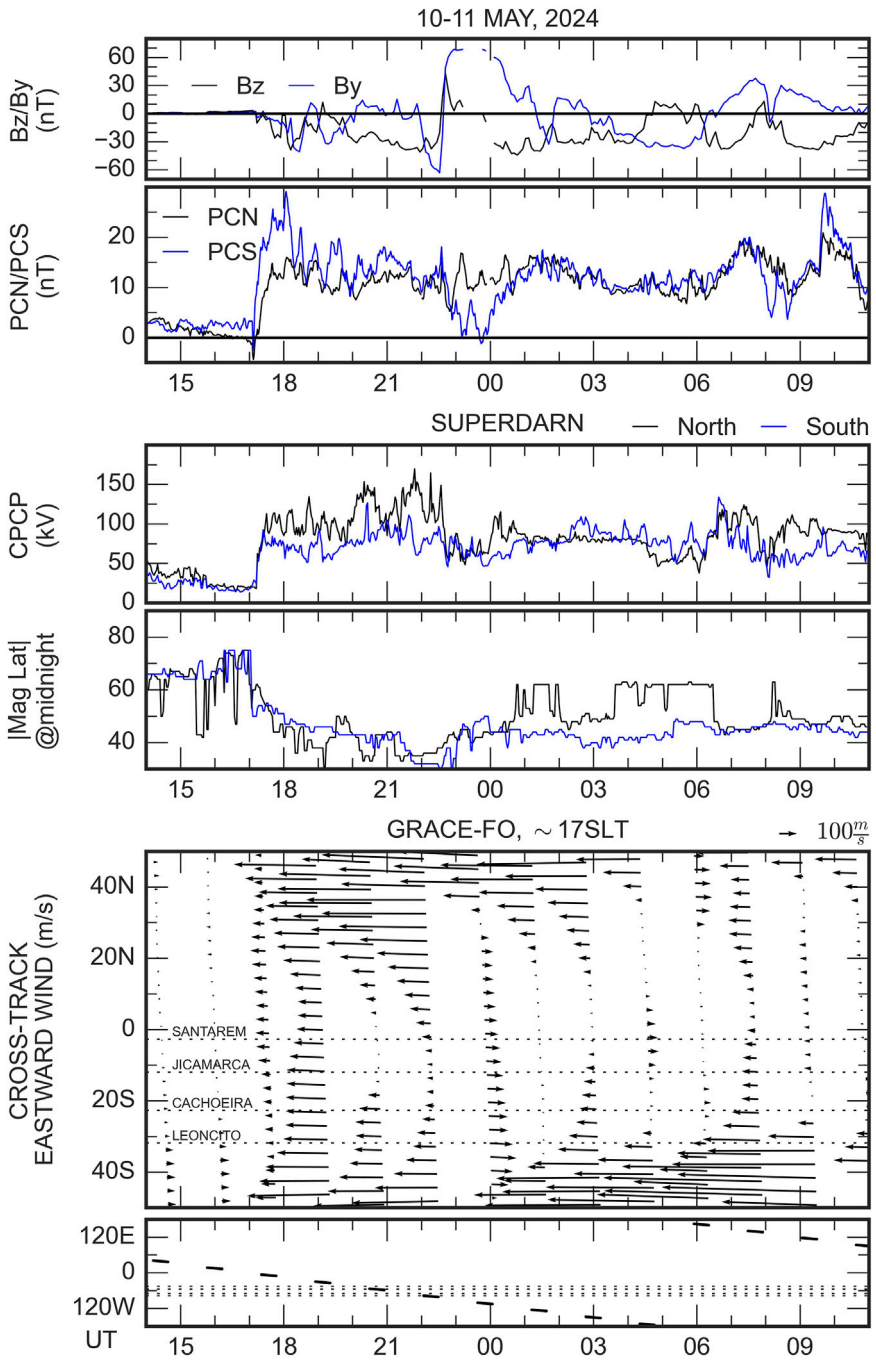

FIGURE 4
Temporal evolution of the thermospheric wind response along the zonal direction during 10–11 May 2024. (From top to bottom) Interplanetary Bz and By Magnetic Fields, Polar Cap Indices, SuperDARN Cross Polar Cap Potential, absolute value of the magnetic latitude of the SuperDARN High Latitude Convection pattern at midnight, and Cross-Track Eastward winds from the GRACE-FO 1 satellite.

(CPCP), and the magnetic latitude expansion of the SuperDARN high-latitude convection pattern at magnetic midnight. The high-latitude convection patterns in both hemispheres exhibited strong equatorward expansions, reaching magnetic latitudes of ~32°S (32°N) at ~22:00 UT (~19:10 UT) in the southern (northern) hemisphere. During the FPI observation period from 00:00 UT to 10:00 UT on 11 May, the southern convection pattern expanded further equatorward, reaching magnetic latitudes of ~40°S, indicating sustained and enhanced high-latitude forcing in the Southern Hemisphere.

The thermospheric winds exhibited westward disturbance effects at all latitudes, with the strongest magnitudes occurring poleward of 30°N and 30°S and reaching ~200 m/s near 19:20 UT on 10 May over the South American sector. These enhanced westward winds persisted up to 22:30 UT, particularly south of 25°S and north of 5°N. Such responses are consistent with previous

observations of storm-time plasma drifts and thermospheric winds driven by solar wind-magnetospheric coupling during storm sudden commencements. Fejer et al. (2024a), (2024b) presented different effects from these drivers and indicated that the equatorial ionosphere exhibits short-lived (~30 min) upward and westward plasma drifts disturbances during sharp dynamic pressure changes at the sudden commencement storms. Xiong et al. (2016) showed a westward (eastward) enhancement in the low latitude thermospheric winds during nighttime (daytime) hours following a sudden increment of solar wind electric field. Navarro et al. (2019) showed similar coupled disturbances in neutral winds and plasma drifts following increment of dynamic pressure over Jicamarca ISR.

As shown in Figure 4, after 23:00 UT the GRACE-FO 1 zonal winds remained predominantly westward at most latitudes, with strongest magnitudes observed south of 20°S and weaker disturbances north of 15°N. A notable exception occurred near 00:00 UT on 11 May, when the winds reversed to eastward over the Pacific sector (~100°W). These eastward winds are consistent with the eastward disturbances observed over Leoncito and with the eastward plasma drifts observed over Jicamarca during the same interval but are opposite to the westward disturbances observed over the East Coast at Cachoeira (Figure 3). This longitudinal asymmetry between the western and eastern sectors of South America coincided with the period of strong IMF By reversal. Furthermore, from 00:00 to 06:00 UT the southern high-latitude convection pattern expanded farther equatorward than its northern counterpart, while GRACE FO 1 observed stronger westward winds south of 30°S. Together, these observations suggest that the enhanced Southern Hemisphere convection and the IMF By may have contributed to the observed hemispheric and longitudinal asymmetries in the thermospheric wind response.

3.4 Thermospheric temperature enhancements

The FPI observations exhibited a persistent and strong temperature enhancement throughout the night and, at certain times, weaker impulsive enhancements. The strong, persistent enhancement is generally attributed to the dissipation of the storm-time high-latitude energy deposition through Joule heating in the ionosphere-thermosphere system (Knipp et al., 2004 and references therein), while the superimposed oscillations are consistent with the arrival of disturbances generated by enhanced high-latitude convection and associated thermospheric dynamics (Emery et al., 1999). Such disturbances can produce localized convergence and divergence of the wind field and corresponding temperature variations (Liu et al., 2023; Gardner and Schunk, 2010).

To further explore the relationship between thermospheric temperature variations and the wind field in the context of TADs, we calculated the horizontal divergence of the wind field over each site following a finite-difference approach. A brief description of this calculation and its physical interpretation is provided in Supplementary Appendix A. Figure 5 compares thermospheric temperatures, horizontal divergence of the wind field, and keograms of detrended TEC centered at each site. Temperature enhancements are highlighted as shaded areas in the top panels and as rectangles in the bottom panels. The figure shows that temperature enhancements are often coincident with periods of wind field convergence, whereas temperature decreases tend to occur during periods of divergence or reduced convergence. The strongest convergence values of 20×10^{-5} s^{-1}, 29×10^{-5} s^{-1}, and 22×10^{-5} s^{-1} were observed at 08:33 UT, 07:40 UT, and 02:20 UT at the Santarem, Cachoeira, and Leoncito sites, respectively.

The highlighted intervals in the bottom panels of Figure 5 are generally indicative of TID signatures, identified as propagating structures in the detrended TEC keograms. For Leoncito and Cachoeira, the keograms indicate disturbances propagating from the Southern Hemisphere with estimated phase speeds of ~620 m/s and ~860 m/s, derived from the slope of the TEC perturbations in the keograms. One disturbance reached Leoncito at ~01:30 UT and later appeared near Jicamarca at ~02:30 UT, while two additional large-scale disturbances arrived near ~07:00 UT and ~10:00 UT. Similar signatures are observed over Cachoeira. Over Santarém, disturbances appear to propagate from both hemispheres. This is particularly evident near ~03:30 UT, when northern- and southern-originating TEC perturbations reached Santarem during a temperature enhancement interval despite relatively weak wind convergence. Additional disturbances are observed near 06:00 UT and 08:30 UT and are consistent with southward-propagating structures previously observed over Cachoeira near 07:45 UT, when the strongest convergence occurred. Notably, recent analysis of mass density observations from a multi-satellite constellation suggest that TAD-related mass density enhancements propagated from high to equatorial latitudes in approximately 3 h (Ai et al., 2026).

Several of these propagating structures also coincided with strong meridional wind surges observed over Santarem. For example, during the intervals centered ~01:50 UT and ~03:15 UT, Santarem exhibited northward and southward wind surges with magnitudes approaching 100 m/s, whereas the corresponding meridional wind perturbations over Leoncito and Cachoeira were generally less than ~50 m/s above their background values. This disturbed interhemispheric circulation pattern is consistent with the presence of TADs, which are frequently accompanied by TID signatures in ionospheric observations (Hunsucker, 1982; Valladares et al., 2025). Previous studies of mass density during this storm point to stronger TAD activity over the southern hemisphere (Ai et al., 2026). Thus, while the TEC perturbations do not directly measure neutral disturbances, the simultaneous occurrence of TEC perturbations, temperature enhancements, wind-field convergence, and meridional wind surges suggests a common disturbance source affecting both the thermosphere and ionosphere. These observations are therefore consistent with the passage of coupled TAD–TID structures through the South American sector during the storm.

The results above are consistent with TID calculations reported by Han et al. (2025) for the same storm event and with previous studies showing that detrended TEC disturbances frequently accompany TIDs and TADs with comparable phase speeds (England et al., 2021; Heelis and Maute, 2020; Souza et al., 2024; and references therein).

The association of temperature enhancements with traveling atmospheric disturbances and periods of wind-field convergence suggests that vertical transport also contributes to the observed thermospheric response. Figure 6 compares the available thermospheric relative vertical winds during the night of 10–11 May over Leoncito and Santarem for the same interval

10.3389/fspas.2026.1830431

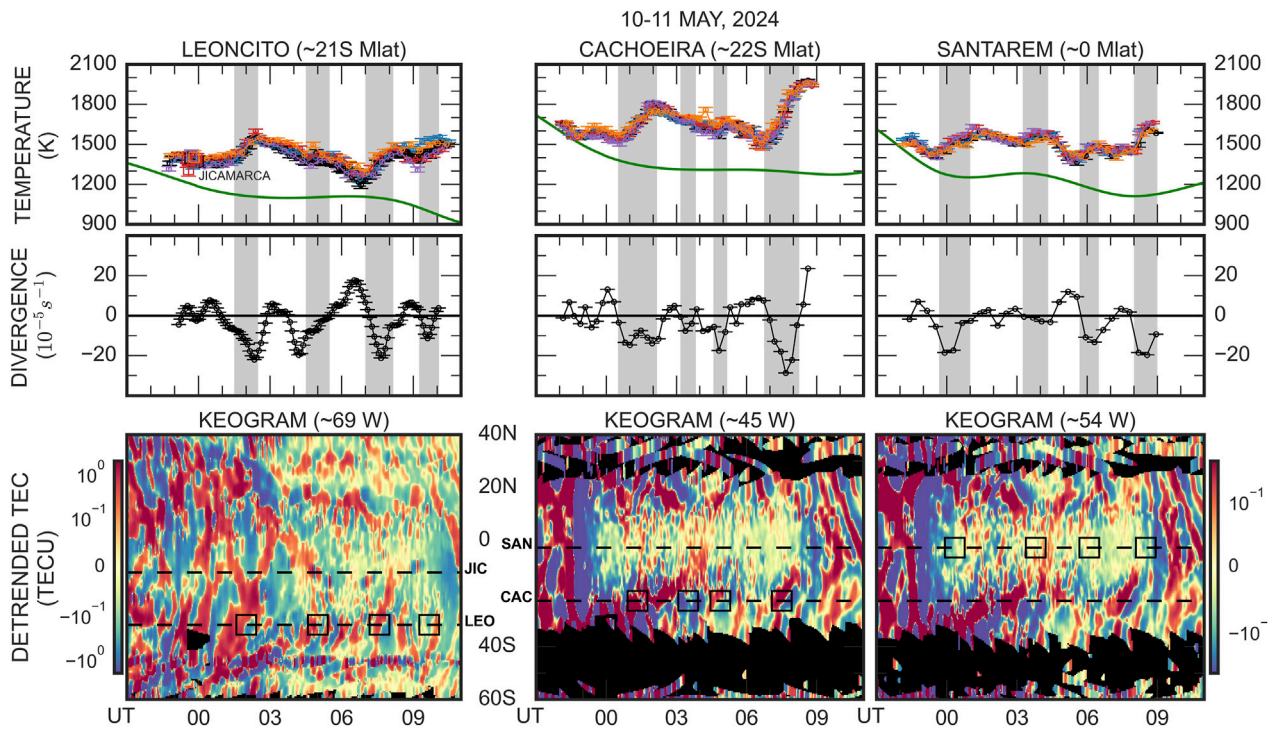

FIGURE 5
(Top) Thermospheric temperature, (middle) horizontal wind divergence and (bottom) Keogram of disturbance propagation of detrended TEC over the western Leoncito site (right), Cachoeira (center) and Santarem (left) sites. Early-night Jicamarca temperature observations are shown along with Leoncito observations. Shaded time windows highlight temperature enhancements.

discussed in Figure 5. Similarly, it is important to note that these relative vertical winds represent relative perturbations derived under the assumption of a zero nightly mean and, therefore, do not represent absolute vertical motions. The Leoncito vertical motion dynamics exhibited strongest downward motions around 02:31 UT and 04:23 UT, coincident with strong convergence values of 20×10^{-5} s^{-1} and 15×10^{-5} s^{-1}, respectively, and with strong and moderate temperature enhancements occurring during the same intervals. Interestingly, the strongest temperature enhancement around 07:30 UT, associated with a convergence of 20×10^{-5} s^{-1}, was accompanied by only a weak downward perturbation. Similar behavior was observed over Santarem, where the strongest downward perturbations occurred near 00:30 UT and 08:30 UT during intervals characterized by strong convergence and enhanced temperatures.

Figure 6 further shows that periods of horizontal wind convergence, marked by brackets, are frequently followed by downward relative vertical wind perturbations, whereas divergence or decreasing convergence is often accompanied by upward perturbations. However, the correspondence between horizontal convergence/divergence, relative vertical motion, and temperature variability is not systematic at all times and does not always exhibit a proportional response. This lack of one-to-one correspondence is evident at both Leoncito and Santarem and suggests that, although convergence and vertical transport may contribute to the observed temperature variability, additional processes associated

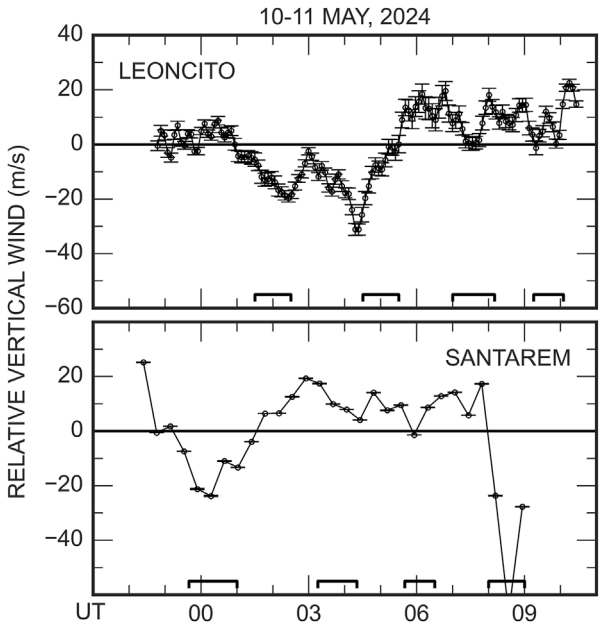

FIGURE 6
Comparison of relative vertical winds over (top) Leoncito, Argentina and (bottom) Santarem, Brazil during the 10–11 May 2024. Brackets mark the shaded periods in Figure 5, corresponding to impulsive temperature enhancements and convergence wind fields.

with storm-time thermospheric dynamics likely also play an important role. Overall, the observations indicate a tendency for convergence intervals to be associated with downward relative vertical wind perturbations, while also highlighting the complexity of the thermospheric response during extreme geomagnetic activity.

4 Discussion

In this section we discuss in more detail the characteristics of the disturbances in the neutral wind and temperatures presented in previous sections.

4.1 Storm-time multi-process effects on thermospheric winds

To further understand the underlying processes and their potential role in the upper atmosphere, we analyzed ionospheric plasma drifts from the Jicamarca ISR. We also used empirical disturbance dynamo drift models to further understand the role of the wind-dynamo driver.

Figure 7 presents the temporal evolution of the upward and eastward plasma drifts during the same interval as the thermospheric wind observations presented in Figures 3, 4. The lower panel included eastward GRACE-FO cross track winds interpolated at Jicamarca latitude and for selected orbits around Jicamarca longitude for a 90° longitude window. The green line represents quiet-time empirical references, namely, the Scherliess and Fejer (1999) quiet-time empirical model for the upward plasma drifts, and a new climatological quiet-time eastward drift model based on extensive Jicamarca ISR observations (Navarro, 2020). The black solid lines show empirical predictions of disturbance dynamo plasma drifts considering 9-h of hourly AE and Kp indices for upward (Navarro et al., 2019) and eastward (Fejer et al., 2005) plasma drifts, respectively. These predictions are climatological representations of the disturbance dynamo disturbances, and their use to extreme cases do not consider potential interactions with concurrent magnetospheric processes such as penetration electric fields or substorms (Maruyama et al., 2005; Fejer and Navarro, 2022), among other potential non-linear storm-time effects. Nevertheless, these empirical models define a useful baseline for comparison.

The drift observations showed a strong upward and westward drift perturbation first between 17:30 and 19:12 UT on 10 May, with peak velocities reaching approximately 80 m/s and 250 m/s respectively. Tulasi Ram et al. (2024) used a wide set of space-borne and ground-based observations and modelling to attribute these effects to strong solar wind dynamic pressure during the interplanetary shock arrival, which produced a dayside magnetopause compression and led to daytime prompt penetration electric fields. Similarly, Fejer et al. (2024b) pointed out that solar wind density and dynamic pressure enhancements can intensity the high-latitude two-cell convection pattern, producing upward and westward daytime equatorial plasma drift perturbations consistent with our observations.

Conversely, the GRACE-FO 1 observations showed westward wind perturbations during the same period. In particular, cross-track winds observed from 17:30 UT to 21:30 UT in the bottom panel of Figure 7 suggest that similar westward dynamics were observed over a longitudinal range spanning the midday sector on the west coast and the late-afternoon sector in the east coast. These wind perturbations occurred shortly after the onset of the plasma drift response. Xiong et al. (2016) used cross-track winds derived from the CHAMP mission to examine the response of thermospheric winds to sudden solar wind variations and found westward (eastward) winds associated with prompt penetration electric fields during 12-18 MLT (00-06 MLT), suggesting ion-drag as a possible coupling mechanism. Other studies have also pointed out a prompt westward wind response near noon at low latitudes during intense magnetic storms (Huang et al., 2021). The temporal correspondence between the observed westward plasma drifts and neutral winds seems consistent with a common magnetospheric forcing associated with the storm sudden commencement, despite the broad longitudinal extent of the observations. Therefore, the GRACE-FO 1 observations are suggestive of a thermospheric response to prompt penetration forcing, although the timing and magnitude of the neutral wind response are likely modulated by ion-neutral coupling and pressure-gradient forces.

The empirical disturbance dynamo drifts show anti-solar quiet-time disturbances in the upward plasma drifts that grow stronger following local sunset, reaching strongest magnitudes of −35 m/s around 01:00 UT while strongly affecting the post-midnight sector. Similarly, westward drift disturbances are weak during sunset and reach strongest effects in the post-midnight sector. The plasma drift observations exhibited strong downward and weak eastward disturbances around sunset, followed by short-lived variations superimposed on the disturbance dynamo background. Such short-lived disturbances after sunset are consistent with prompt penetration electric fields associated with solar wind-magnetosphere dynamo and with magnetospheric substorm activity, both of which have been shown to produce rapid and short-duration variations in equatorial zonal and vertical plasma drifts (Fejer et al., 1979; 1990; Fejer and Scherliess, 1995; Fejer et al., 20224b). This interpretation is further supported by empirical predictions from the Prompt Penetration Electric Field model of Manoj and Maus (2012), which indicate enhanced storm-time electric field variability during these intervals (not shown). A few studies have focused on the magnetospheric driver of these disturbances during this storm (Astafyeva et al., 2025; Huang et al., 2025; Zhang et al., 2025). Other storm-time processes, including atmospheric wave activity and field-line conductivity disturbances, may also contribute to the observed short-timescale variability.

Figure 7 also show that, starting at 01:04 UT 11 May, the zonal drift disturbances over Jicamarca had consecutive eastward peaks of ~220 m/s at 04:15 and 06:35 UT, and a westward peak of ~150 m/s at 08:00 UT. These short-lived magnetospheric effects typically occur on time scales of minutes to a few hours and are often superposed on the longer-lasting disturbance dynamo signatures during geomagnetic storms (Fejer et al., 2005; Fejer and Navarro, 2022; Zhang et al., 2023). Several other studies discussed the substorm and super substorm activity effects during this storm over the ionosphere (Hajra et al., 2025; Zou et al., 2025) but a detailed characterization of substorm effects are beyond the scope of this study.

While these processes likely contribute to the short-lived features observed in the plasma drifts, the thermospheric wind response examined here follows the same short-time scale effects

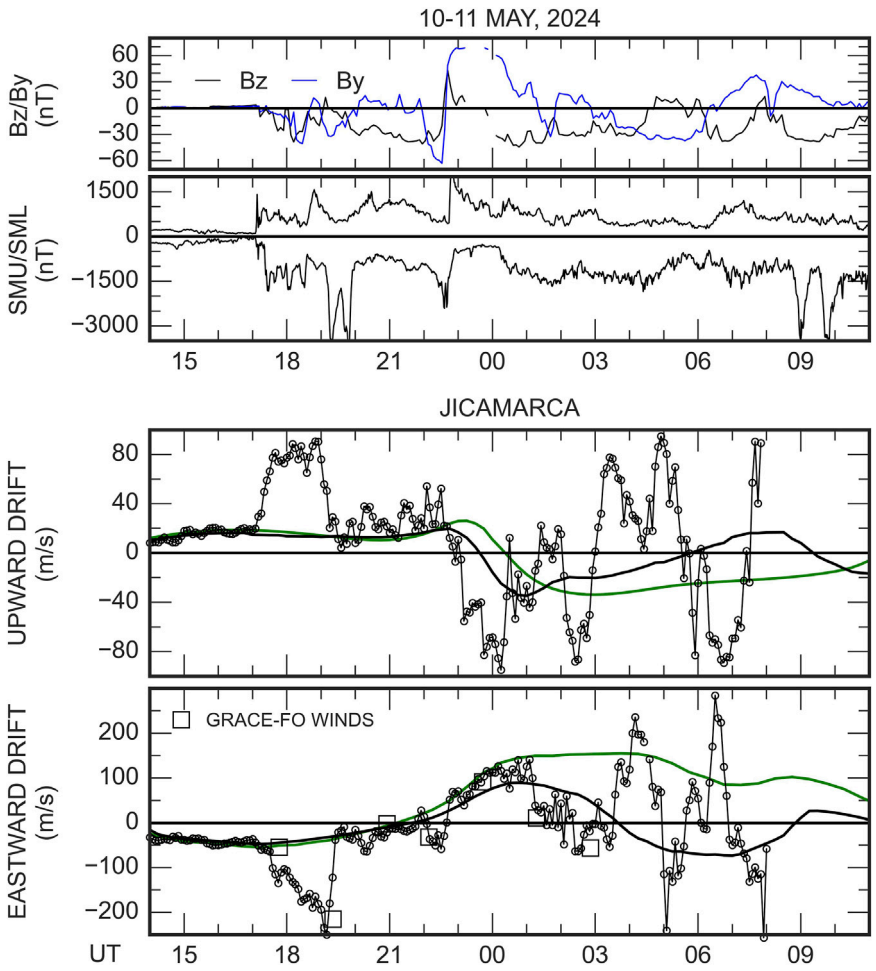

FIGURE 7
Solar Wind parameters, geomagnetic indices, equatorial plasma drift and wind observations, and comparison of quiet and disturbance dynamo drift empirical models during 10–11 May 2024. (Top panels) Interplanetary Bz and By Magnetic Fields and SuperMAG Auroral Electrojet Upper (SMU) and Lower (SML) indices. (Bottom panels) Upward and eastward drifts observations over Jicamarca together with the climatological quiet time patterns (green curves) and empirical disturbance dynamo patterns (black curves) described in the text.

and the longer-term disturbance winds driven by storm-time energy input. GRACE-FO 1 wind observations at equatorial latitudes followed closely the plasma drift observations as shown in the bottom panel of Figure 7. They appear to lag the plasma drifts by ~8 min during the zonal drift response of the sudden storm commencement. Similarly, the FPI wind observations in Figure 3 exhibited weak eastward disturbances at ~04:00 UT and ~08:00 UT consistent with the strong eastward drift disturbances observed in the eastward drifts. This suggests the superposition of a long-lasting thermospheric response associated with storm-time Joule heating and shorter-timescale magnetospheric-driven wind disturbances, with the former providing the dominant contribution to the overall thermospheric wind field.

An important aspect regarding the plasma-neutral coupling is the significant difference in magnitude of the short-lived zonal drift disturbances at 04:00 UT and 06:30 UT 11 May reaching 250 m/s and 350 m/s eastward with respect to the disturbance dynamo drift baseline, and the zonal winds disturbances at about the same time with amplitudes of about 40–50 m/s eastward in both Santarem and Leoncito FPIs. This period was also characterized by a strong uplifting of the F-layer height during this period (Carmo et al., 2024). Similarly, a few studies using mass density satellite observations have reported an expansion of the thermosphere and their effects during the same storm period (Parker and Linares, 2024). This storm-time expansion of the upper atmosphere leads to strong enhancements of mass density observations in constant-altitude observing platforms such as accelerometers on satellites (Lei et al., 2010; Prolss, 2005). One possible implication of this expansion is that the volume emission rate (VER) profile and peak altitude for the OI (6,300 A) airglow line may be modified, particularly, during periods when the plasma drift observations are occurring at altitudes above 500 km after 04:00 UT 11 May. Previous studies have shown that the OI VER profile and peak altitude are sensitive to the F-region electron density distribution, including variations in NmF2, hmF2, and the overall layer shape (Link and Cogger, 1988; Nicolls et al., 2006; Vlasov et al., 2005). The storm-time variations in the VER OI emission profile and peak altitude would have played a role into the weak coupling exhibited by these zonal observations, in contrast

with weaker storms which showed stronger coupling during much weaker magnetospheric disturbances (Navarro and Fejer, 2020). It is also important to note the difference in the observing geometry of the GRACE-FO 1 and FPI platforms since they sample different altitude regions of the thermosphere. The FPI observations are primarily weighted by the OI (630.0 nm) emission profile generally assumed at ~250 km, whereas the GRACE-FO 1 cross-track winds represent bulk neutral motion near ~475 km altitude. Consequently, comparisons between the two datasets should be interpreted with caution, as altitude-dependent ion-drag coupling, pressure-gradient forcing, and thermospheric inertia may produce different wind responses at these heights and during these storm-time conditions. Nevertheless, the datasets provide complementary information regarding the large-scale storm-time evolution of the neutral atmosphere.

The overall behavior of nigh-time FPI disturbance wind dynamics is consistent with similar storm-time FPI wind studies over the Peruvian equatorial sector (Meriwether, 2008; Navarro and Fejer, 2019; 2020), the African low-latitude sector (Malki et al., 2018), and with storm-time cross-track wind observations (Xiong et al., 2015). However, although the zonal winds observed at Leoncito and Cachoeira were both westward, they exhibited opposite zonal wind response, becoming increasingly westward over Leoncito while weakening over Cachoeira. The initial eastward velocities observed at Leoncito are consistent with eastward plasma drift velocities over Jicamarca, as well as with the west-to-east reversal showed by GRACE-FO 1 cross-track winds over the Pacific.

Our empirical disturbance dynamo drift model, together with previous empirical equatorial disturbance wind models (Navarro and Fejer, 2019; 2020), indicates that the strongest equatorial zonal wind and drift disturbances typically occur in the post-midnight sector, with relatively weak disturbances during the early-night hours. The observed zonal wind evolution over Leoncito and Santarem is consistent with this behavior. However, the interpretation is complicated by the large IMF By reversal that occurred during the storm main phase during the late-afternoon hours. Recent studies have shown that this reversal played a key role in modulating ionospheric convection and hemispheric asymmetries throughout the magnetosphere–ionosphere system. In particular, Ohtani et al. (2025) demonstrated that the IMF By reversal strongly affected daytime conductivity, plasma density, and plasma drifts, and that global simulations successfully reproduced the associated westward-to-eastward reversal of the midday high-latitude auroral electrojet. Such large-scale changes in the high-latitude current system can also influence low-latitude electrodynamics through the modulation of disturbance dynamo electric fields and the generation of prompt penetration electric fields (Fejer et al., 2024b). Therefore, while the observed wind evolution is consistent with expected disturbance dynamo behavior, part of the response may also reflect the influence of storm-time convection changes associated with the IMF By reversal. Other processes involving drift and wind-driven perturbations at magnetic conjugate locations may contribute to the dynamics observed over Cachoeira. Previous studies (e.g., Fejer,1993; Takami et al., 1996; Foster and Rideout, 2007 among others) suggest that these electrodynamic effects are often controlled by the summer magnetic conjugate location, rather than by the local winter conjugate location, due to seasonal conductivity asymmetries, and that the relative timing of sunset between conjugate locations can further modulate this coupling.

4.2 Storm-time effects on thermospheric temperature

During the night of 10–11 May, thermospheric temperatures over the east and west coast of South America exhibited similar temporal variability of strong and steady enhancements and overlapping oscillations as shown by Figure 3. The thermospheric temperature variability has often been associated with release of energy at high-latitude region through Joule heating, and different geomagnetic indices has been used to estimate this parameter, including the Polar Cap Index. The Polar Cap Index has been associated with energy inputs in the high latitude ionosphere due to ionospheric Hall and field-aligned currents at the poleward edge of the auroral oval, and it has been used as a proxy for the interplanetary electric field merging with Earth's Magnetic Field (Chun et al., 1999). This index has also been correlated with hemispheric Joule Heating production rate for several geomagnetic storms analyzed under the Assimilative Mapping of Electrodynamics (AMIE) procedure (Chun et al., 1999; Chun et al., 2002). These studies have found quadratic empirical relationship between Joule heating and Polar Cap Index as in Knipp et al. (2005) while other found linear relationships with Auroral Electrojet (Lu et al., 1995). Note also that the AMIE framework does not consider neutral winds effects associated with Joule heating (Cooper et al., 1995). Other proxies related the Cross Polar Cap Potential to the Polar Cap through linear empirical relationships during storm-time conditions (Chun et al., 2002). For the present event, the sustained enhancements in the CPCP, Polar Cap, and SMU/SML indices during the main phase of the storm are consistent with prolonged high-latitude energy deposition and with the elevated thermospheric temperatures observed throughout the night. In particular, enhancements from 22:00 UT to 00:00 UT, 02:30 UT, and 06:00 to 07:00 UT in these indices seem to be aligned with propagating disturbances from the southern hemisphere and observed in Leoncito and Cachoeira. Similar enhancements over the northern counterpart of these indices could be also related to the short-lived surges over Santarem. However, the weaker signal over this region preclude a clearer association.

Figures 5, 6 suggest that some of the observed thermospheric variability may be associated with impulsive Joule heating across the high-latitude ionosphere-thermosphere region that generated TAD/TID disturbances transporting heated air equatorward and reorganizing the neutral wind field affecting its divergence and potentially contributing to adiabatic heating/cooling at low and equatorial latitudes and the associated vertical motion (Fuller-Rowell et al., 1994; Rodger et al., 2001; Smith, 2000). However, not all temperature enhancements are associated with clear TID signatures or strong convergence, suggesting that multiple processes contribute to the observed thermospheric variability.

Bruinsma and Forbes (2010) used accelerometers measurements to analyze the characteristics of Large Scale Traveling Atmospheric Disturbances (LSTAD) during mild and strong geomagnetic storms. They found that the propagation speed and magnitude was strongly dependent on Joule heating with average propagation

speeds of ~600 m/s. These results are similar to those regularly observed in TID events during storms and reported by keograms (Fuller-Rowell et al., 1994; Prolss and Očko, 2000; Shiokawa et al., 2002, and references therein). Biondi and Sipler (1985) used similar instrumentation over Brazil and found storm-time vertical winds velocities associated with temperature variations which was also attributed to gravity wave modulations of the equatorial thermospheric flow. In general, the overall thermospheric temperature dynamics exhibited by our observations is consistent with similar studies (Fuller-Rowell et al., 1997; Meriwether, 2008; Prolss et al., 1973).

As indicated in Section 3.4, the horizontal divergence/convergence of the wind field and relative vertical motion is not systematic at all times and not always associated with a proportional response in the temperature variations. Moreover, the comparison of temperature variations due to the adiabatic heating effects and wind field divergence alone explored in the Supplementary Appendix A suggests that the underlying assumptions might not be met across latitudes and altitudes. The adiabatic heating effects assumes that the wind field divergence is reasonably constant about all height across the upper atmosphere whereas there are probably significant variations of horizontal wind divergence with height along the TAD pathway. Furthermore, the divergence estimates are derived from observations at a single altitude range and therefore do not resolve the vertical structure of the disturbance. Moreover, the competing processes of long-lasting disturbance winds and sudden magnetospheric forcing might create these differences at different latitudes.

Nevertheless, Richmond and Matsushita (1975), Prolss (1997), Prolss (2011), and others attributed the commonly observed storm-time composition changes due to vertical winds or upwelling following expansion of neutral gas due to the Joule heating of the high-latitude upper atmosphere. This process has been proposed to evolve into Hadley-type circulation cell following continuous high-latitude storm-time upwelling, transporting composition, wind and temperature disturbances equatorward. Our observations of relative vertical motion and temperature variations suggest that this description could be applicable during several of the observed heating intervals. However, because the relative vertical winds represent perturbations relative to the nightly mean Doppler shift, any sustained background vertical circulation associated with prolonged Joule heating and thermospheric expansion would be most likely absorbed into the reference level and therefore cannot be directly assessed with the present observations. Thus, these observations should be viewed as supporting evidence of storm-time oscillatory responses rather than direct measurements of the background circulation itself.

Notably, and on top of these short-time responses potentially related to TADs, the overall temporal evolution of the relative vertical variations shows a similar trend with the large-scale variations of the vertical plasma drifts, with a 2-h lagged response over Leoncito than over Santarem. This broad correspondence is suggestive of coupled ionosphere-thermosphere variability, although it does not by itself demonstrate propagation or a global circulation response.

Overall, the observations suggest a two-component thermospheric response during the 10–11 May 2024 superstorm. The first component consists of a persistent background heating characterized by elevated temperatures throughout the night and consistent with sustained high-latitude energy deposition inferred from the CPCP, Polar Cap, and auroral electrojet indices. Superimposed on this background are shorter-timescale perturbations that are often associated with TAD/TID signatures, wind-field convergence, and relative vertical wind variations. Although these transient disturbances do not exhibit a one-to-one correspondence with the observed temperature enhancements, they likely contribute to the observed oscillatory variability through a combination of dynamical and electrodynamical processes. Clearly, the complex processes behind these observations require further theoretical and empirical studies.

5 Summary and conclusion

We presented a coordinated ground-based thermospheric neutral wind and temperature observations over the South American sector during the extreme 10–11 May 2024 geomagnetic storm. These measurements were complemented by equatorial plasma drifts from the Jicamarca Incoherent Scatter Radar and cross-track neutral winds from the GRACE-FO 1 satellite. The combined dataset was used to investigate the storm-time effects of magnetospheric and high-latitude forcing into the thermospheric dynamics, and to identify the dominant processes driving the observed neutral disturbances.

1. A prompt response to the sudden storm commencement was observed between 17:30 and 19:12 UT on 10 May, characterized by a strong upward and westward plasma drifts at the magnetic equator over the west coast of South America and concurrent westward neutral wind disturbances in GRACE-FO 1 cross-track winds. During this period, the neutral response exhibited substantial longitudinal variability across low latitudes, and the observations suggest that the disturbances weakened earlier near the magnetic equator.
2. Nighttime observations revealed exceptionally strong and persistent thermospheric disturbances throughout the storm main phase and early recovery, with pronounced longitudinal and latitudinal variability. The zonal winds exhibited opposite storm-time evolution over the western and eastern sectors of South America, becoming increasingly westward over Leoncito while weakening and eventually reversing over Cachoeira. At the magnetic equator, the Santarem winds transitioned from eastward to westward along the night reaching ~100 m/s by early morning. GRACE-FO 1 observations over the Pacific exhibited large-scale westward winds and a later reversal to eastward winds that was generally consistent with the Jicamarca plasma drifts observations.
3. The meridional winds over Leoncito and Cachoeira were found to be moderately disturbed with short-lived weak surges at about the same time for both stations. Conversely, the meridional winds over Santarem showed strong interhemispheric surges of ~100 m/s in the pre- and midnight sectors and mild surges in the post-midnight sector. These were generally consistent with TAD-related

processes and with signatures exhibited by Keograms of detrended TEC.

4. The thermospheric temperatures remained strongly enhanced throughout the night, with superimposed impulsive variations. The sustained temperatures enhancement is consistent with storm-time energy deposition at high latitudes, while the shorter-timescale variability appears to reflect the combined influence of multiple processes, including traveling atmospheric disturbances and changes in thermospheric circulation. Although some temperature enhancements occurred during intervals of enhanced wind convergence and TID signatures, consistent with possible adiabatic heating and cooling associated with the reorganization of the thermospheric wind field during the passage of TAD-related disturbances, the correspondence was not systematic. This suggests that not a single mechanism fully explains the observed temperature variability.
5. Periods of enhanced horizontal convergence were frequently accompanied by downward relative vertical perturbations, suggesting that storm-time reorganization of the horizontal wind may have contributed to the observed temperature variability. However, the correspondence between convergence, relative vertical motion, and temperature was not systematic, and the relative vertical winds represent perturbations relative to a nightly mean rather than absolute vertical motion. This behavior highlights the complex, three-dimensional nature of storm-time thermospheric dynamics.
6. Comparison with Jicamarca plasma drifts shows that prompt penetration and substorm-related electric fields contributed to short-lived ionospheric disturbances, while longer-lasting disturbance dynamo and disturbance wind processes contributed to the thermospheric response. GRACE-FO 1 cross-track winds and ground-based FPI observations together showed similar storm-time variability to the plasma drifts, although important differences in timing, and longitudinal behavior were also observed. These observations suggest a weak zonal plasma-neutral coupling under combined electrodynamic and thermodynamic forcing during the 10–11 May. For periods of strong differences between plasma drifts and neutral winds, storm-time changes in the OI (6,300 Å) emission profile and peak altitude may have contributed to the observed differences, although other factors such as observing geometry, ion-drag efficiency, neutral inertia, and altitude-dependent thermospheric responses are also likely important.

Overall, this study demonstrates that the May 2024 superstorm produced a highly structured thermospheric response over South America, driven by a combination of sustained high-latitude energy input, traveling atmospheric disturbances, and complex electrodynamic forcing associated with disturbance dynamo and magnetospheric processes. The observations support a multi-timescale response consisting of persistent nighttime heating superimposed with transient perturbations in the neutral winds and temperatures. These results emphasize the importance of coordinated ground-based and satellite observations to resolve the temporal and spatial evolution of storm-time thermospheric dynamics. Further observational and modeling studies are required to better quantify the relative roles of electrodynamic and neutral forcing, the vertical structure of storm-time heating and divergence, and the origin of the observed longitudinal asymmetries during extreme geomagnetic events.

Data availability statement

This analysis utilizes GNSS TEC observations that are published in the MIT/CEDAR Madrigal database. Madrigal archives the line-of-sight TEC data, which are the basis of TID analysis. These data are available at http://cedar.openmadrigal.org. Once in the system, please click the tab "Access data" and choose "Distributed ground-based satellite receivers" and "World-wide GNSS receiver network" to enter individual days of observations. The ISR drift data were acquired and processed by the Geophysical Institute of Peru (IGP) and are publicly available through the IGP Madrigal Database (https://www.igp.gob.pe/observatorios/radio-observatorio-jicamarca/madrigal/). The specific data version used in this study is archived at https://w3id.org/cedar?experiment_list=experiments/2024/jmp/10may24D. The Cachoeira FPI data is available through http://cedar.openmadrigal.org. Leoncito raw data will be made available by the authors. A viewer for the wind data can be found in https://swx-trec.com/airglow/. The analyzed Leoncito winds and temperatures and Jicamarca drifts data presented in this study is available at https://doi.org/10.25810/xe1e-b436. The geomagnetic indices are available through https://supermag.jhuapl.edu/ and from the National Centers for Environmental Information of the National Oceanic and Atmospheric Administration (https://ngdc.noaa.gov), and the solar wind data from the Space Physica Data Facility (https://omniweb.gsfc.nasa.gov). The raw SuperDARN data for 2024 are available from SuperDARN data mirror servers through Globus transfer protocol (https://github.com/SuperDARNCanada/globus). To obtain the equatorward boundary of high-latitude convection (HMB), these data were processed using the standard Radar Software Toolkit (RST) written in C (Thomas et al., 2025).

Author contributions

LN: Writing – original draft, Writing – review and editing. BF: Writing – review and editing. JM: Writing – review and editing. CM: Writing – review and editing. SZ: Writing – review and editing. RK: Writing – review and editing. JS: Writing – review and editing. DS: Writing – review and editing. CS: Writing – review and editing. ED: Writing – review and editing. PP: Writing – review and editing.

Funding

The author(s) declared that financial support was received for this work and/or its publication. This work was supported

by NSF CEDAR AGS-2230438 and NASA ECIP 80NSSC23K1066 awards. JM was supported by NSF-CEDAR AGS-2230439. CM was supported by NSF-CEDAR AGS-2230440. SRZ was supported by NSF awards AGS-2149698 and AGS-2437054, NASA grants 80NSSC21K1310 and 80NSSC22K1013, and AFOSR grant A9550-23-1-0474. PP is supported by the Canadian Space Agency (CSA) under grant 21SUSTMRPI. The authors acknowledge the use of SuperDARN data. SuperDARN is a collection of radars funded by the national scientific funding agencies of Australia, Canada, China, France, Italy, Japan, Norway, South Africa, United Kingdom and United States of America. The FPIs in Brazil are supported by The Brazilian Ministry of Science, Technology and Innovation, Brazilian Space Agency and CNPq (Grant 311840/2022-1) and by NSF award number 2431743. GNSS TEC data processing and Madrigal database system are provided to the community by MIT Haystack Observatory under the NSF grant AGS-2504079 support. The Jicamarca Radio Observatory is a facility of the Instituto Geofisico del Peru operated with support from the NSF AGS-2213849 through Cornell University.

Acknowledgments

The authors thank the Director and personnel of CASLEO (Complejo Astronomico El Leoncito) for their continued support of the BU Fabry-Perot Interferometer. LN sincerely thanks A. D. Richmond for useful discussions and valuable assistance with the paper.

Conflict of interest

Author RK was employed by Computational Physics Inc.

The remaining author(s) declared that this work was conducted in the absence of any commercial or financial relationships that could be construed as a potential conflict of interest.

The handling editor AB declared a past co-authorship with the author DS.

The author SR-Z declared that they were an editorial board member of Frontiers at the time of submission. This had no impact on the peer review process and the final decision.

Generative AI statement

The author(s) declared that generative AI was not used in the creation of this manuscript.

Any alternative text (alt text) provided alongside figures in this article has been generated by Frontiers with the support of artificial intelligence and reasonable efforts have been made to ensure accuracy, including review by the authors wherever possible. If you identify any issues, please contact us.

Publisher's note

All claims expressed in this article are solely those of the authors and do not necessarily represent those of their affiliated organizations, or those of the publisher, the editors and the reviewers. Any product that may be evaluated in this article, or claim that may be made by its manufacturer, is not guaranteed or endorsed by the publisher.

Supplementary material

The Supplementary Material for this article can be found online at: https://www.frontiersin.org/articles/10.3389/fspas.2026.1830431/full#supplementary-material

References

Ai, J., Zhang, X., Li, Y., Sun, Y., Bai, W., Guo, X., et al. (2026). Global thermospheric density response to the May 2024 extreme storm: TianMu-1 constellation observations. *Earth Planet. Phys.* 10, 105–116. doi: 10.26464/epp2026003

Astafyeva, E., Maletckii, B., Förster, M., Ouar, I. D., Huba, J. D., Hairston, M. R., et al. (2025). Electrodynamic and ionospheric puzzles of the 10–11 May 2024 geomagnetic superstorm. *J. Geophys. Res. Space Phys.* 130 (5), e2024JA033284. doi: 10.1029/2024JA033284

Biondi, M. A., and Sipler, D. P. (1985). Horizontal and vertical winds and temperatures in the equatorial thermosphere: measurements from Natal, Brazil during August–September 1982. *Planet. Space Sci.* 33 (7), 817–823. doi: 10.1016/0032-0633(85)90035-2

Blanc, M., and Richmond, A. D. (1980). The ionospheric disturbance dynamo. *J. Geophys. Res. Space Phys.* 85 (A4), 1669–1686. doi: 10.1029/JA085iA04p01669

Bruinsma, S. L., and Forbes, J. M. (2010). Large-scale traveling atmospheric disturbances (LSTADs) in the thermosphere inferred from CHAMP, GRACE, and SETA accelerometer data. *J. Atmos. Solar-Terrestrial Phys.* 72 (13), 1057–1066. doi: 10.1016/j.jastp.2010.06.010

Carmo, C. S., Dai, L., Wrasse, C. M., Barros, D., Takahashi, H., Figueiredo, C. O. B., et al. (2024). Ionospheric response to the extreme 2024 mother's day geomagnetic storm over the Latin American sector. *Space Weather* 22 (12), e2024SW004054. doi: 10.1029/2024SW004054

Chisham, G., Lester, M., Milan, S. E., Freeman, M. P., Bristow, W. A., Grocott, A., et al. (2007). A decade of the super dual auroral radar network (SuperDARN): scientific achievements, new techniques and future directions. *Surv. Geophys.* 28 (1), 33–109. doi: 10.1007/s10712-007-9017-8

Chun, F. K., Knipp, D. J., McHarg, M. G., Lu, G., Emery, B. A., Vennerstrøm, S., et al. (1999). Polar cap index as a proxy for hemispheric joule heating. *Geophys. Res. Lett.* 26 (8), 1101–1104. doi: 10.1029/1999GL900196

Chun, F. K., Knipp, D. J., McHarg, M. G., Lacey, J. R., Lu, G., and Emery, B. A. (2002). Joule heating patterns as a function of polar cap index. *J. Geophys. Res. Space Phys.* 107 (A7), 8-1–8-9. doi: 10.1029/2001JA000246

Cooper, M. L., Clauer, C. R., Emery, B. A., Richmond, A. D., and Winningham, J. D. (1995). A storm time assimilative mapping of ionospheric electrodynamics analysis for the severe geomagnetic storm of November 8–9, 1991. *J. Geophys. Res.* 100 (A10), 19329–19342. doi: 10.1029/95JA01402

Coster, A. J., Goncharenko, L., Zhang, S.-R., Erickson, P. J., Rideout, W., and Vierinen, J. (2017). GNSS observations of ionospheric variations during the 21 August 2017 solar eclipse. *Geophys. Res. Lett.* 44 (24), 12041–12048. doi: 10.1002/2017GL075774

Emery, B. A., Lathuillere, C., Richards, P. G., Roble, R. G., Buonsanto, M. J., Knipp, D. J., et al. (1999). Time dependent thermospheric neutral response to the 2–11 November 1993 storm period. *J. Atmos. Solar-Terrestrial Phys.* 61 (3-4), 329–350. doi: 10.1016/S1364-6826(98)00137-0

England, S. L., Greer, K. R., Zhang, S.-R., Evans, S., Solomon, S. C., Eastes, R. W., et al. (2021). First comparison of traveling atmospheric disturbances observed in the middle thermosphere by global-scale observations of the limb and disk to traveling ionospheric disturbances seen in ground-based total electron content observations. *J. Geophys. Res. Space Phys.* 126 (6), e2021JA029248. doi: 10.1029/2021JA029248

Fejer, B. G. (1993). F region plasma drifts over arecibo: solar cycle, seasonal, and magnetic activity effects. *J. Geophys. Res.* 98 (A8), 13645–13652. doi: 10.1029/93JA00953

Fejer, B. G., and Navarro, L. A. (2022). First observations of equatorial ionospheric electric fields driven by storm-time rapidly recurrent magnetospheric substorms. *J. Geophys. Res. Space Phys.* 127 (12), e2022JA030940. doi: 10.1029/2022JA030940

Fejer, B. G., and Scherliess, L. (1995). Time dependent response of equatorial ionospheric electric fields to magnetospheric disturbances. *Geophys. Res. Lett.* 22 (7), 851–854. doi: 10.1029/95GL00390

Fejer, B. G., Gonzales, C. A., Farley, D. T., Kelley, M. C., and Woodman, R. F. (1979). Equatorial electric fields during magnetically disturbed conditions 1. The effect of the interplanetary magnetic field. *J. Geophys. Res. Space Phys.* 84 (A10), 5797–5802. doi: 10.1029/JA084iA10p05797

Fejer, B. G., Kelley, M. C., Senior, C., de la Beaujardiere, O., Holt, J. A., Tepley, C. A., et al. (1990). Low- and mid-latitude ionospheric electric fields during the January 1984 GISMOS campaign. *J. Geophys. Res.* 95 (A3), 2367–2377. doi: 10.1029/JA095iA03p02367

Fejer, B. G., Souza, J. R., Santos, A. S., and Costa Pereira, A. E. (2005). Climatology of F region zonal plasma drifts over Jicamarca. *J. Geophys. Res. Space Phys.* 110 (A12). doi: 10.1029/2005JA011324

Fejer, B. G., Jensen, J. W., and Su, S.-Y. (2008). Seasonal and longitudinal dependence of equatorial disturbance vertical plasma drifts. *Geophys. Res. Lett.* 35 (20). doi: 10.1029/2008GL035584

Fejer, B. G., Blanc, M., and Richmond, A. D. (2017). Post-storm middle and low-latitude ionospheric electric fields effects. *Space Sci. Rev.* 206 (1), 407–429. doi: 10.1007/s11214-016-0320-x

Fejer, B. G., Laranja, S. R., and Condor, P. (2024a). Multi-process driven unusually large equatorial perturbation electric fields during the April 2023 geomagnetic storm. *Front. Astronomy Space Sci.* 11, 1351735. doi: 10.3389/fspas.2024.1351735

Fejer, B. G., Navarro, L. A., and Chakrabarty, D. (2024b). Recent results and outstanding questions on the response of the electrodynamics of the low latitude ionosphere to solar wind and magnetospheric disturbances. *Front. Astronomy Space Sci.* 11, 1471140. doi: 10.3389/fspas.2024.1471140

Flores, R., Manay, I., Condor, P., Kuyeng, K., Scipión, D., and Milla, M. (2026). Monitoring the equatorial ionosphere with the upgraded unattended mode at Jicamarca. *J. Geophys. Res. Space Phys.* 131, e2026JA035193. doi: 10.1029/2026JA035193

Foster, J. C., and Rideout, W. (2007). Storm enhanced density: magnetic conjugacy effects. *Ann. Geophys.* 25, 1791–1799. doi: 10.5194/angeo-25-1791-2007

Fuller-Rowell, T. J., Codrescu, M. V., Moffett, R. J., and Quegan, S. (1994). Response of the thermosphere and ionosphere to geomagnetic storms. *J. Geophys. Res. Space Phys.* 99 (A3), 3893–3914. doi: 10.1029/93JA02015

Fuller-Rowell, T. J., Codrescu, M. V., Fejer, B. G., Borer, W., Marcos, F., and Anderson, D. N. (1997). Dynamics of the low-latitude thermosphere: quiet and disturbed conditions. *J. Atmos. Solar-Terrestrial Phys. Ninth Int. Symposium Equat. Aeronomy* 59 (13), 1533–1540. doi: 10.1016/S1364-6826(96)00154-X

Gardner, L. C., and Schunk, R. W. (2010). Generation of traveling atmospheric disturbances during pulsating geomagnetic storms. *J. Geophys. Res.* 115, A08314. doi: 10.1029/2009JA015129

Greenwald, R. A., Baker, K. B., Dudeney, J. R., Pinnock, M., Jones, T. B., Thomas, E. C., et al. (1995). DARN/SuperDARN. *Space Sci. Rev.* 71 (1), 761–796. doi: 10.1007/BF00751350

Hajra, R., Tsurutani, B. T., Lakhina, G. S., Lu, Q., and Du, A. (2024). Interplanetary causes and impacts of the 2024 May superstorm on the geosphere: an overview. *Astrophysical J.* 974 (2), 264. doi: 10.3847/1538-4357/ad7462

Hajra, R., Tsurutani, B. T., Lu, Q., Du, A., and Lakhina, G. S. (2025). Supersubstorms during the May 2024 superstorm. *J. Space Weather Space Clim.* 15, 51. doi: 10.1051/swsc/2025047

Han, T., Le, H., Yang, Y., Li, W., Sun, W., Ma, H., et al. (2025). Characteristics of large-scale traveling ionospheric disturbances during the 10 May 2024 geomagnetic storm. *Space Weather* 23, e2024SW004283. doi: 10.1029/2024SW004283

Harding, B. J., Gehrels, T. W., and Makela, J. J. (2014). Nonlinear regression method for estimating neutral wind and temperature from Fabry-Perot interferometer data. *Appl. Opt.* 53 (4), 666–673. doi: 10.1364/AO.53.000666

Harding, B. J., Makela, J. J., Meriwether, J. W., Fisher, D. J., Buriti, R. A., and Medeiros, A. F. (2017). Atmospheric scattering effects on ground-based Fabry–Perot interferometer measurements of thermospheric vertical winds. *J. Geophys. Res. Space Phys.* 122 (1), 579–592. doi: 10.1002/2017JA023942

Hayakawa, H., Ebihara, Y., Mishev, A., Koldobskiy, S., Kusano, K., Bechet, S., et al. (2024). The solar and geomagnetic storms in May 2024: a flash data report. *Astrophy. J.* 979 (1), 49. doi: 10.3847/1538-4357/ad9335

Heelis, R. A., and Maute, A. (2020). Challenges to understanding the earth's ionosphere and thermosphere. *J. Geophys. Res. Space Phys.* 125 (7), e2019JA027497. doi: 10.1029/2019JA027497

Heppner, J. P., and Maynard, N. C. (1987). Empirical high-latitude electric field models. *J. Geophys. Res. Space Phys.* 92 (A5), 4467–4489. doi: 10.1029/JA092iA05p04467

Hładczuk, N. A., van den Ijssel, J., Kodikara, T., Siemes, C., and Visser, P. (2024). GRACE-FO radiation pressure modelling for accurate density and crosswind retrieval. *Adv. Space Res.* 73 (5), 2355–2373. doi: 10.1016/j.asr.2023.12.059

Huang, C.-S., Zhang, Y., Wang, W., Lin, D., and Wu, Q. (2021). Low-latitude zonal ion drifts and their relationship with subauroral polarization streams and auroral return flows during intense magnetic storms. *J. Geophys. Res. Space Phys.* 126, e2021JA030001. doi: 10.1029/2021JA030001

Huang, F., Lei, J., Yue, X., Li, Z., Zhang, N., Cai, Y., et al. (2025). Interplay of gravity waves and disturbance electric fields to the abnormal ionospheric variations during the 11 May 2024 superstorm. *AGU Adv.* 6 (1), e2024AV001379. doi: 10.1029/2024AV001379

Hunsucker, R. D. (1982). Atmospheric gravity waves generated in the high-latitude ionosphere: a review. *Rev. Geophys.* 20 (2), 293–315. doi: 10.1029/RG020i002p00293

Karan, D. K., Martinis, C. R., Daniell, R. E., Eastes, R. W., Wang, W., McClintock, W. E., et al. (2024). GOLD observations of the merging of the southern crest of the equatorial ionization anomaly and Aurora during the 10 and 11 May 2024 mother's day super geomagnetic storm. *Geophys. Res. Lett.* 51 (15), e2024GL110632. doi: 10.1029/2024GL110632

Kerr, R. B., Kapali, S., Harding, B. J., Riccobono, J., Migliozzi, M. A., Souza, J. R., et al. (2023). Spectral contamination of the 6300 Å emission in single-etalon fabry-perot interferometers. *J. Geophys. Res. Space Phys.* 128 (9), e2023JA031601. doi: 10.1029/2023JA031601

Knipp, D. J., Tobiska, W. K., and Emery, B. A. (2004). Direct and indirect thermospheric heating sources for solar cycles 21–23. *Sol. Phys.* 224 (1), 495–505. doi: 10.1007/s11207-005-6393-4

Knipp, D. J., Welliver, T., McHarg, M. G., Chun, F. K., Tobiska, W. K., and Evans, D. (2005). Climatology of extreme upper atmospheric heating events. *Adv. Space Res.* 36 (12), 2506–2510. doi: 10.1016/j.asr.2004.02.019

Kudeki, E., Bhattacharyya, S., and Woodman, R. F. (1999). A new approach in incoherent scatter F region E x B drift measurements at Jicamarca. *J. Geophys. Res. Space Phys.* 104 (A12), 28145–28162. doi: 10.1029/1998JA900110

Lei, J., Thayer, J. P., Burns, A. G., Lu, G., and Deng, Y. (2010). Wind and temperature effects on thermosphere mass density response to the November 2004 geomagnetic storm. *J. Geophys. Res. Space Phys.* 115 (A5). doi: 10.1029/2009JA014754

Link, R., and Cogger, L. L. (1988). A reexamination of the O I 6300-Å nightglow. *J. Geophys. Res.* 93 (A9), 9883–9892. doi: 10.1029/JA093iA09p09883

Liu, B., Liu, J., Liu, X., Zhong, J., Li, S., and Li, Q. (2023). Dynamics of thermospheric traveling atmospheric disturbance during a geomagnetic storm. *J. Geophys. Res. Space Phys.* 128, e2023JA031448. doi: 10.1029/2023JA031448

Lu, G., Richmond, A. D., Emery, B. A., and Roble, R. G. (1995). Magnetosphere-ionosphere-thermosphere coupling: effect of neutral winds on energy transfer and field-aligned current. *J. Geophys. Res. Space Phys.* 100 (A10), 19643–19659. doi: 10.1029/95JA00766

Malki, K., Bounhir, A., Benkhaldoun, Z., Makela, J. J., Vilmer, N., Fisher, D. J., et al. (2018). Ionospheric and thermospheric response to the 27–28 February 2014 geomagnetic storm over North Africa. *Ann. Geophys.* 36 (4), 987–998. doi: 10.5194/angeo-36-987-2018

Martinis, C., Meriwether, J. W., and Navarro, L. A. (2025). Thermospheric wind and temperature observations from El leoncito observatory in southern South America. *Front. Astronomy Space Sci.* 12, 1666096. doi: 10.3389/fspas.2025.1666096

Manoj, C., and Maus, S. (2012). A real-time forecast service for the ionospheric equatorial zonal electric field. *Space Weather* 10, S09002. doi: 10.1029/2012SW000825

Maruyama, N., Richmond, A. D., Fuller-Rowell, T. J., Codrescu, M. V., Sazykin, S., Toffoletto, F. R., et al. (2005). Interaction between direct penetration and disturbance dynamo electric fields in the storm-time equatorial ionosphere. *Geophys. Res. Lett.* 32, L17105. doi: 10.1029/2005GL023763

Massoud, A. A., Abubakar, A. A., Rodrigues, F. S., Kuyeng, K. M., Inoñán, M., and Scipión, D. E. (2026). On vertical plasma drift measurements made by a new medium power incoherent scatter radar (MP ISR) mode at the Jicamarca radio observatory. *Adv. Space Res.* 77 (9), 9651–9661. doi: 10.1016/j.asr.2026.03.009

Mazaudier, C., and Venkateswaran, S. V. (1988). Delayed ionospheric effects of March 22, 1979 studied by the sixth coordinated data analysis workshop (CDAW-6). *Ann. Geophys.* 8 (511), 1–8. Available online at: https://hal.science/hal-01009312v1.

Meriwether, J. W. (2008). "Thermospheric dynamics at low and mid-latitudes during magnetic storm activity," in *Midlatitude Ionospheric Dynamics and Disturbances* (American Geophysical Union AGU), 201–219. doi: 10.1029/181GM19

Meriwether, J., Faivre, M., Fesen, C., Sherwood, P., and Veliz, O. (2008). New results on equatorial thermospheric winds and the midnight temperature maximum. *Ann. Geophys.* 26, 447–466. doi: 10.5194/angeo-26-447-2008

Meriwether, J. W., Makela, J. J., Huang, Y., Fisher, D. J., Buriti, R. A., Medeiros, A. F., et al. (2011). Climatology of the nighttime equatorial thermospheric winds and temperatures over Brazil near solar minimum. *J. Geophys. Res. Space Phys.* 116 (A4). doi: 10.1029/2011JA016477

Navarro, L. (2020). *Storm-Time Equatorial Thermospheric Dynamics and Electrodynamics*. Logan, Utah: Utah State University. doi: 10.26076/a730-2625

Navarro, L. A., and Fejer, B. G. (2019). Storm-time thermospheric winds over Peru. *J. Geophys. Res. Space Phys.* 124 (12), 10415–10427. doi: 10.1029/2019JA027256

Navarro, L. A., and Fejer, B. G. (2020). Storm-time coupling of equatorial nighttime F region neutral winds and plasma drifts. *J. Geophys. Res. Space Phys.* 125 (9), e2020JA028253. doi: 10.1029/2020JA028253

Navarro, L. A., Fejer, B. G., and Scherliess, L. (2019). Equatorial disturbance dynamo vertical plasma drifts over jicamarca: bimonthly and solar cycle dependence. *J. Geophys. Res. Space Phys.* 124 (6), 4833–4841. doi: 10.1029/2019JA026729

Nicolls, M. J., Vlasov, M. N., Kelley, M. C., and Shepherd, G. G. (2006). Discrepancy between the nighttime molecular ion composition given by the international reference ionosphere model and airglow measurements at low latitudes. *J. Geophys. Res.* 111, A03304. doi: 10.1029/2005JA011216

Nishitani, N., Ruohoniemi, J. M., Lester, M., Baker, J. B. H., Koustov, A. V., Shepherd, S. G., et al. (2019). Review of the accomplishments of mid-latitude super dual auroral radar network (SuperDARN) HF radars. *Prog. Earth Planet. Sci.* 6 (1), 27. doi: 10.1186/s40645-019-0270-5

Ohtani, S., Zou, Y., Merkin, V. G., Wiltberger, M., Pham, K. H., Raptis, S., et al. (2025). Ground magnetic response to an extraordinary IMF BY flip during the May 2024 storm: travel time from the magnetosheath to dayside high latitudes. *J. Geophys. Res. Space Phys.* 130 (5), e2024JA033691. doi: 10.1029/2024JA033691

Parker, W. E., and Linares, R. (2024). Satellite drag analysis during the May 2024 gannon geomagnetic storm. *J. Spacecr. Rockets* 61 (5), 1412–1416. doi: 10.2514/1.A36164

Paul, K. S., Haralambous, H., Moses, M., and Tripathi, S. C. (2025). Effects of the October 2024 storm over the global ionosphere. *Remote Sens.* 17 (13), 2329. doi: 10.3390/rs17132329

Prolss, G. W. (1991). Thermosphere-ionosphere coupling during disturbed conditions. *J. Geomagnetism Geoelectr.* 43 (Suppl. 1), 537–549. doi: 10.5636/jgg.43.Supplement1_537

Prolss, G. W. (1997). "Magnetic storm associated perturbations of the upper atmosphere," in *Magnetic Storms* (American Geophysical Union AGU), 227–241. doi: 10.1029/GM098p0227

Prolss, G. W. (2005). "Space weather effects in the upper atmosphere: low and middle latitudes," in *Space Weather: The Physics Behind a Slogan*. Editors K. Scherer, H. Fichtner, B. Heber, and U. Mall (Springer), 193–214. doi: 10.1007/978-3-540-31534-6_6

Prolss, G. W. (2011). Density perturbations in the upper atmosphere caused by the dissipation of solar wind energy. *Surv. Geophys.* 32 (2), 101–195. doi: 10.1007/s10712-010-9104-0

Prolss, G. W., and Očko, M. (2000). Propagation of upper atmospheric storm effects towards lower latitudes. *Adv. Space Res. Space Weather Phys. Appl.* 26 (1), 131–135. doi: 10.1016/S0273-1177(99)01039-X

Prolss, G. W., Najita, K., and Yuen, P. C. (1973). Heating of the low-latitude upper atmosphere caused by the decaying magnetic storm ring current. *J. Atmos. Terr. Phys.* 35 (10), 1889–1901. doi: 10.1016/0021-9169(73)90062-7

Richmond, A. D., and Matsushita, S. (1975). Thermospheric response to a magnetic substorm. *J. Geophys. Res.* 80 (19), 2839–2850. doi: 10.1029/JA080i019p02839

Richmond, A. D., Peymirat, C., and Roble, R. G. (2003). Long-lasting disturbances in the equatorial ionospheric electric field simulated with a coupled magnetosphere-ionosphere-thermosphere model. *J. Geophys. Res. Space Phys.* 108 (A3). doi: 10.1029/2002JA009758

Rodger, A. S., Wells, G. D., Moffett, R. J., and Bailey, G. J. (2001). The variability of joule heating, and its effects on the ionosphere and thermosphere. *Ann. Geophys.* 19 (7), 773–781. doi: 10.5194/angeo-19-773-2001

Ruohoniemi, J. M., and Baker, K. B. (1998). Large-scale imaging of high-latitude convection with super dual auroral radar network HF radar observations. *J. Geophys. Res. Space Phys.* 103 (A9), 20797–20811. doi: 10.1029/98JA01288

Savitzky, A., and Golay, M. J. E. (1964). Smoothing and differentiation of data by simplified least squares procedures. *Anal. Chem.* 36 (8), 1627–1639. doi: 10.1021/ac60214a047

Scherliess, L., and Fejer, B. G. (1999). Radar and satellite global equatorial F region vertical drift model. *J. Geophys. Res. Space Phys.* 104 (A4), 6829–6842. doi: 10.1029/1999JA900025

Shiokawa, K., Otsuka, Y., Ogawa, T., Balan, N., Igarashi, K., Ridley, A. J., et al. (2002). A large-scale traveling ionospheric disturbance during the magnetic storm of 15 September 1999. *J. Geophys. Res. Space Phys.* 107 (A6), 5-1–5-11. doi: 10.1029/2001JA000245

Singh, R., Scipión, D. E., Kuyeng, K., Condor, P., De La Jara, C., Velasquez, J. P., et al. (2024). Ionospheric disturbances observed over the Peruvian sector during the mother's day storm (G5-Level) on 10–12 May 2024. *J. Geophys. Res. Space Phys.* 129 (11), e2024JA033003. doi: 10.1029/2024JA033003

Smith, R. W. (2000). The global-scale effect of small-scale thermospheric disturbances. *J. Atmos. Solar-Terrestrial Phys.* 62 (17-18), 1623–1628. doi: 10.1016/S1364-6826(00)00123-1

Souza, J. R., Dandenault, P., Santos, A. M., Riccobono, J., Migliozzi, M. A., Kapali, S., et al. (2024). Impacts of storm electric fields and traveling atmospheric disturbances over the americas during 23–24 April 2023 geomagnetic storm: experimental analysis. *J. Geophys. Res. Space Phys.* 129, e2024JA032698. doi: 10.1029/2024JA032698

Sutton, E. K., Forbes, J. M., and Nerem, R. S. (2005). Global thermospheric neutral density and wind response to the severe 2003 geomagnetic storms from CHAMP accelerometer data. *J. Geophys. Res. Space Phys.* 110 (A9). doi: 10.1029/2004JA010985

Takami, T., Oliver, W. L., Richmond, A. D., and Fukao, S. (1996). Ionospheric drift similarities at magnetic conjugate and nonconjugate locations. *J. Geophys. Res.* 101 (A7), 15773–15782. doi: 10.1029/96JA01316

Themens, D. R., Elvidge, S., McCaffrey, A., Jayachandran, P. T., Coster, A., Varney, R. H., et al. (2024). The high latitude ionospheric response to the major May 2024 geomagnetic storm: a synoptic view. *Geophys. Res. Lett.* 51 (19), e2024GL111677. doi: 10.1029/2024GL111677

Thomas, E. G., Burrell, A. G., Ponomarenko, P. V., Bland, E. C., Sterne, K. T., Rohel, R. A., et al. (2025). *Superdarn Radar Software Toolkit (RST) 5.1 (V5.1)*. Zenodo. doi: 10.5281/zenodo.4435150

Tripathi, S. C., Haralambous, H., and Biswas, T. (2025). Ionospheric variability during the 10 October 2024 geomagnetic storm: a regional analysis across Europe. *Atmosphere* 16 (9), 1029. doi: 10.3390/atmos16091029

Tsugawa, T., Saito, A., and Otsuka, Y. (2004). A statistical study of large-scale traveling ionospheric disturbances using the GPS network in Japan. *J. Geophys. Res. Space Phys.* 109 (A6). doi: 10.1029/2003JA010302

Tulasi Ram, S., Veenadhari, B., Dimri, A. P., Bulusu, J., Bagiya, M., Gurubaran, S., et al. (2024). Super-intense geomagnetic storm on 10–11 May 2024: possible mechanisms and impacts. *Space Weather.* 22 (12), e2024SW004126. doi: 10.1029/2024SW004126

Valladares, C. E., Chen, Y.-J., Bukowski, A., Adhya, P., Anderson, P. C., Dey, S., et al. (2025). Measurements of LSTID and LSTAD using TEC and GOCE data. *Front. Astronomy Space Sci.* 12, 1517762. doi: 10.3389/fspas.2025.1517762

Vlasov, M. N., Nicolls, M. J., Kelley, M. C., Smith, S. M., Aponte, N., and González, S. A. (2005). Modeling of airglow and ionospheric parameters at Arecibo during quiet and disturbed periods in October 2002. *J. Geophys. Res.* 110, A07303. doi: 10.1029/2005JA011074

Wang, X., Aa, E., Chen, Y., Zhang, J., Zhu, Y., Cai, L., et al. (2025). Midlatitude neutral wind response during the mother's day super-intense geomagnetic storm in 2024 using observations from the Chinese Meridian project. *J. Geophys. Res. Space Phys.* 130 (4), e2024JA033574. doi: 10.1029/2024JA033574

Woodman, R. F. (1970). Vertical drift velocities and east-west electric fields at the magnetic equator. *J. Geophys. Res.* 75 (31), 6249–6259. doi: 10.1029/JA075i031p06249

Xiong, C., Lühr, H., and Fejer, B. G. (2015). Global features of the disturbance winds during storm time deduced from CHAMP observations. *J. Geophys. Res. Space Phys.* 120 (6), 5137–5150. doi: 10.1002/2015JA021302

Xiong, C., Lühr, H., and Fejer, B. G. (2016). The response of equatorial electrojet, vertical plasma drift, and thermospheric zonal wind to enhanced solar wind input. *J. Geophys. Res. Space Phys.* 121 (6), 5653–5663. doi: 10.1002/2015JA022133

Zhang, S.-R., Erickson, P. J., Foster, J. C., Holt, J. M., Coster, A. J., Makela, J. J., et al. (2015). Thermospheric poleward wind surge at midlatitudes during great storm intervals. *Geophy. Res. Lett.* 42 (13), 5132–5140. doi: 10.1002/2015gl064836

Zhang, S.-R., Erickson, P. J., Goncharenko, L. P., Coster, A. J., Rideout, W., and Vierinen, J. (2017). Ionospheric bow waves and perturbations induced by the 21 August 2017 solar eclipse. *Geophys. Res. Lett.* 44 (24), 12067–12073. doi: 10.1002/2017GL076054

Zhang, S.-R., Coster, A. J., Erickson, P. J., Goncharenko, L. P., Rideout, W., and Vierinen, J. (2019). Traveling ionospheric disturbances and ionospheric perturbations associated with solar flares in September 2017. *J. Geophys. Res. Space Phys.* 124 (7), 5894–5917. doi: 10.1029/2019JA026585

Zhang, S.-R., Nishimura, Y., Vierinen, J., Lyons, L. R., Knipp, D. J., Gustavsson, B. J., et al. (2023). Simultaneous global ionospheric disturbances associated with penetration electric fields during intense and minor solar and geomagnetic disturbances. *Geophys. Res. Lett.* 50 (19), e2023GL104250. doi: 10.1029/2023GL104250

Zhang, R., Liu, L., Yang, Y., Li, W., Zhao, X., Yoshikawa, A., et al. (2024). Ionosphere responses over Asian-Australian and American sectors to the 10–12 May 2024 superstorm. *J. Geophys. Res. Space Phys.* 129, e2024JA033071. doi: 10.1029/2024JA033071

Zhang, R., Liu, L., Yue, X., Zhang, J., Zhang, N., Chen, Y., et al. (2025). The penetration electric fields during the 10 May 2024 superstorm observed by ISRs over Sanya and Jicamarca. *Geophys. Res. Lett.* 52, e2024GL114543. doi: 10.1029/2024GL114543

Zou, Y., Ohtani, S., Gjerloev, J. W., Anderson, B. J., Waters, C. L., Wang, C.-P., et al. (2025). Are supersubstorms substorms? Extreme nightside auroral electrojet activities during the May 2024 geomagnetic storm. *J. Geophys. Res. Space Phys.* 130 (3), e2024JA033303. doi: 10.1029/2024JA033303